A STUDY OF THE LIGHT EMISSION FROM SiN_x FILMS

A STUDY OF THE LIGHT EMISSION FROM SiN_x FILMS

By

JORDAN TYLER ANSTEY, B.Sc.

B.Sc. (McMaster University) 2009

A Thesis
Submitted to the School of Graduate Studies
in Partial Fulfillment of the Requirements
for the Degree
Master of Applied Science

McMaster University

MASTER OF APPLIED SCIENCE (2011) McMaster University
Engineering Physics Hamilton, Ontario

TITLE: A Study of the Light Emission from SiN_x Films

AUTHOR: Jordan Tyler Anstey (McMaster University)

SUPERVISORS: Professor P. Mascher, Professor A. Knights

NUMBER OF PAGES: viii, 99

Abstract

The use of silicon in optoelectronics is gaining interest due to the possibility of applications such as optical interconnects. Though much progress has been made, the search still continues for the elusive silicon light emitter, which could make the prospect of silicon photonics a reality. This work has examined the properties of a potential candidate for a silicon-based light source: silicon nanocluster embedded silicon nitride films. In addition, the optical properties of Ce-doped silicon nitride films with and without nanoclusters were investigated.

The silicon nitride films exhibited bright luminescence that peaked after annealing at temperatures between 600^{o}C and 800^{o}C, depending on how the nitrogen was introduced during the deposition; the more silicon rich films (for which a dispersion ring was used) peaked at a lower anneal temperature. As well, the photoluminescence (PL) spectra of the plasma and dispersion ring samples had main peaks at about 650 nm and 750 nm, respectively. Lastly, all the spectra exhibited a redshift at higher anneal temperatures. These observations support the opinion that silicon nanoclusters were formed from the excess silicon. However, TEM imaging did not show conclusive evidence of their existence.

The Ce-doped films displayed even brighter luminescence. When the cerium was implanted into stoichiometric silicon nitride the emission was solely from Ce^{3+} ions, with the PL spectra being centred at 450 nm. However, when the cerium was implanted into the silicon rich film, there appears to be emission from both Ce^{3+} ions and silicon

nanoclusters as the broad PL spectrum ranges from about 450 nm to 750 nm. After annealing at 1000^{o}C there is a shift in the PL spectrum and the emission is almost exclusively from Ce^{3+} ions. Both films exhibited a strong increase in PL intensity with annealing above 1000^{o}C, but it is not known if this is due to the formation of cerium silicate, which has been suggested before with Ce-doped silicon oxide films.

Acknowledgements

There are many people who helped me greatly the last couple of years and this thesis would not be possible without them. First, I would like to offer my sincere gratitude to my supervisors, Dr. Andy Knights and Dr. Peter Mascher. Their guidance was invaluable to my learning and my development as a researcher.

Though many fellow grad students have been a source of support the last couple of years, there are two in particular that I would like to thank. First, Tyler Roschuk, for teaching me to use the PL system before he left. Second, Patrick Wilson, for many helpful discussions and for performing my XAS experiments and aiding me in the analysis of the XAS spectra.

In the labs several technicians assisted me in fabricating my samples. In particular, I would like to thank Evgueni Chelomensev, Doris Stevanovic, and Jacek Wojcik for helping to deposit my films, analyze them with the ellipsometer, implant them with ions, and showing me how to use the metallization system.

I am grateful for the staff members at the CCEM for all their assistance with my work. Wen He Gong, Carmen Andrei, Fred Pearson, and Julia Huang all helped me immensely with preparing my samples, viewing them on the microscopes, and analyzing the images. As well, I also want to thank the summer students Sneha Bernard and Connor Wilson for helping teach me to do TEM sample prep.

Lastly, I want to thank my wife Stephanie for her continuing support.

Table of Contents

List of Figures

Chapter 1: Introduction

1.1 Silicon Photonics

Silicon is the most widely used material in microelectronics, and a vast infrastructure is already in place for the processing of it [1]. However, due to its indirect band gap and insignificant electro-optic coefficient, silicon is not an ideal candidate for optical devices [2]. Instead, III-V semiconductor materials with direct band gaps such as GaAs and InP have played a significant role in photonics. In the field of photonics, it would be advantageous to make use of the mature silicon manufacturing methods; silicon wafers have the lowest cost per unit area and the highest crystal quality of any semiconductor material [3]. Silicon could potentially be used in applications such as displays, solid state lighting [4] and mid-infrared photonic devices [3]. However, the real driving force behind silicon photonics research is creating optical interconnects on an integrated photonic circuit (Fig. 1.1) [5].

For several decades microprocessors have been becoming increasingly more complex, by both the continued miniaturization of the fundamental component of a microprocessor, the transistor, and the number of transistors roughly doubling every two years according to Moore's Law [6] (Fig. 1.2). By scaling down the size of transistors, they are able to operate at higher frequencies than in the past. However, another consequence of scaling down the size of the transistors is that we are approaching a point

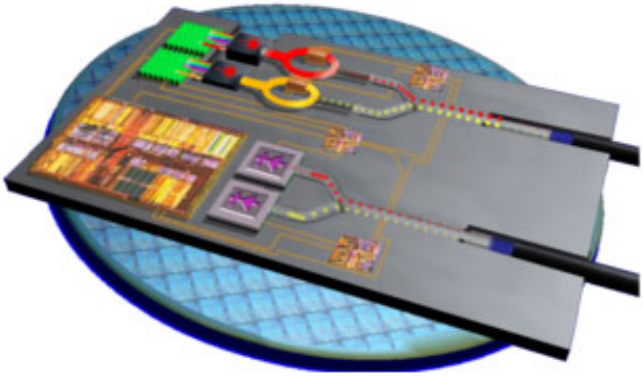

Figure 1.1: A possible design for silicon photonics integration [5]

where parasitic RC time delays are the dominant factor in the performance of a microprocessor. Indeed, for gate lengths less than about 200 nm, the delay is determined by the wiring delay rather than the gate switching time [7]. In addition, the total interconnection length on a chip is getting longer and longer, on the order of several kilometres per cm^2. The architecture of microprocessors is also becoming more complex, with an increasing number of layers. All these issues cause delay problems such as RC coupling, signal latency, signal cross-talk, and RL delays. A possible solution is to replace the traditional metal interconnects with optical interconnects. The goal of silicon photonics is to be able to fabricate everything on silicon; to integrate all the optical components on a chip with Si CMOS compatibility.

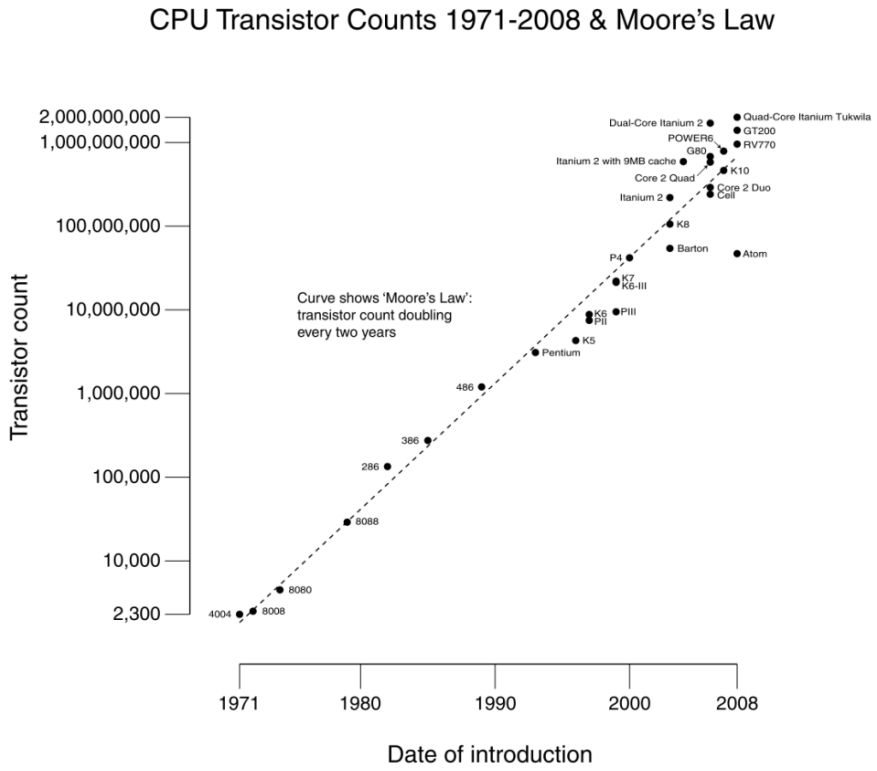

Figure 1.2: Number of transistors in CPUs increasing according to Moore's Law [8]

The requirements for the realization of optical interconnects, as outlined in the 2003 International Technology Roadmap for Semiconductors (ITRS) are [9]:

1) A high efficiency, high switching rate laser source, monolithically integratable into Si CMOS at low cost
2) A low power modulator, monolithically integratable into Si CMOS at low cost
3) Low power, high efficiency, small size optical detectors monolithically integratable into Si CMOS at low cost

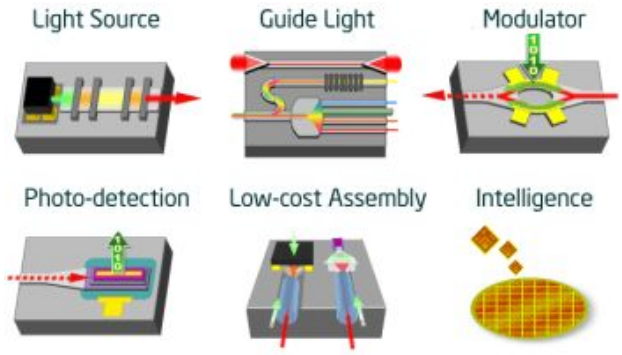

Figure 1.3: The required components for an integrated silicon photonic chip [5]

The essential components for a photonic integrated silicon chip are shown in Fig. 1.3. Silicon-based waveguides [10], modulators [11], and detectors [12] have all been demonstrated. The last remaining obstacle is to develop a silicon-based light source.

The reason for silicon being an inefficient light emitter is its indirect band gap, which requires both a phonon and a photon to facilitate an optical process. However, by spatially confining the charge carriers in silicon there is a spread in the electrons' momentum and the need for a phonon is relaxed, thereby increasing the efficiency of light emission. This was first experimentally demonstrated in 1990 by Canham [13] using porous silicon. Since then, silicon nanocluster-embedded silicon oxide has become a popular material for silicon-based light sources [14]. Optical gain has even been observed in silicon nanocrystals (crystalline nanoclusters) in SiO_2 [15], providing hope that a silicon-based laser may indeed be possible using this platform.

Though silicon oxide was initially the typical host matrix for silicon nanoclusters, silicon nitride has gained interest due to its lower tunnelling barrier, resulting in easier electron and hole transport to the nanoclusters [16]. This work has exclusively used silicon nitride as the host matrix for silicon nanoclusters. In recent years visible

electroluminescence has been demonstrated with silicon nanocrystals embedded in amorphous silicon nitride [17], suggesting that a silicon-based LED could be made for use in solid state lighting and displays.

In addition to the generally broad nanocluster emission, the dielectrics can also be doped with rare earths which emit at a specific wavelength [18]. Erbium is a strong candidate for use in telecommunications due to its emission at 1535 nm, while other rare earths emit in the visible range and can be used for LEDs.

1.2 Outline of Thesis

The overall objective of this thesis is to analyze the luminescent properties of silicon nanocluster embedded dielectrics, specifically silicon nitride films, as well as Ce-doped silicon nitrides. These materials are possible candidates for silicon based optical interconnects or LEDs in the future.

In Chapter 2 the band structure of semiconductors is discussed, as well as the physics of light emission. Next, it is explained how quantum confinement can be used to increase the radiative efficiency of indirect band gap materials like silicon. Lastly, an overview of recent developments in the fields of silicon nanocluster embedded dielectrics and rare earth doped dielectrics is presented.

Chapter 3 discusses the methods used to fabricate the films used in this work. Two different types of chemical vapour deposition were used, as well as an ion implanter to implant excess silicon into the films and a rapid thermal processor to anneal the films.

The characterization techniques used to analyze the luminescence, composition, and bonding structure of the films, are presented in Chapter 4. This includes

photoluminescence spectroscopy, Rutherford backscattering spectrometry, transmission electron microscopy, and x-ray absorption spectroscopy.

The results and discussion are presented in Chapter 5.

To finish, a summary of the results of the work is given in Chapter 6, as well as an outline of possible future research projects.

Chapter 2: Light Emission from Silicon

The optical properties of a semiconductor such as silicon are directly related to the detailed band structure of the material, therefore this chapter will begin with a discussion on the band theory of semiconductors, which explains why silicon in its bulk state is an inefficient light emitter.

The band structure is a material property that cannot be changed, so bulk silicon is always an inefficient light emitter. However, by simply reducing silicon to a small volume the light emission can be increased drastically. This chapter will explain how quantum confinement is achieved (using silicon nanoclusters embedded in a dielectric) and how it can improve the efficiency of light emission. Lastly, current research in the field of silicon nanocluster embedded dielectrics as well as rare earth doped dielectrics will be discussed.

2.1 Band Structure of Semiconductors

Semiconductors are often described as being materials with resistivities lying between those of insulators and metals. Though this is true, it is a very simplistic definition and does not adequately explain the reasons for all of the unique properties of semiconductors. The band theory of solids provides a more accurate way of viewing solids, and is crucial to the understanding of semiconductor properties. Band theory states that the electron states in a solid lie in energy bands rather than discrete energy levels as

in a single atom [19]. Within these bands there are many states available to the electrons, but there are forbidden regions separating the bands where no electron states exist. This region between bands is known as the band gap.

With this theory, the difference between metals, insulators, and semiconductors can be seen when one looks at how the electron states in the bands are filled. Electrons are fermions and therefore obey the Fermi-Dirac distribution

$$n(E) = \frac{1}{e^{(E-\mu)/k_B T} + 1} \tag{2.1}$$

At 0 K the electrons will fill all the lowest energy states up to the Fermi level, or chemical potential μ. If the Fermi level lies in the middle of an energy band so that many states are still available to allow for current, this is a metal. If the Fermi level lies in the band gap so that there are only completely full and completely empty bands and no available states for current, this is an insulator. The highest filled band is called the valence band and the lowest empty band is called the conduction band. A semiconductor then is an insulator with a small enough band gap energy that an appreciable amount of electrons are thermally excited from the valence band to the conduction band at room temperature. Typical semiconductor band gap energies range from ~1 eV to ~4 eV.

When plotting the band structure of a semiconductor not only does the energy have to be taken into account but also the momentum, or wave vector $\vec{k}$. This can result in a very complex surface in phase space, as shown in the band structure of silicon (Fig. 2.1)

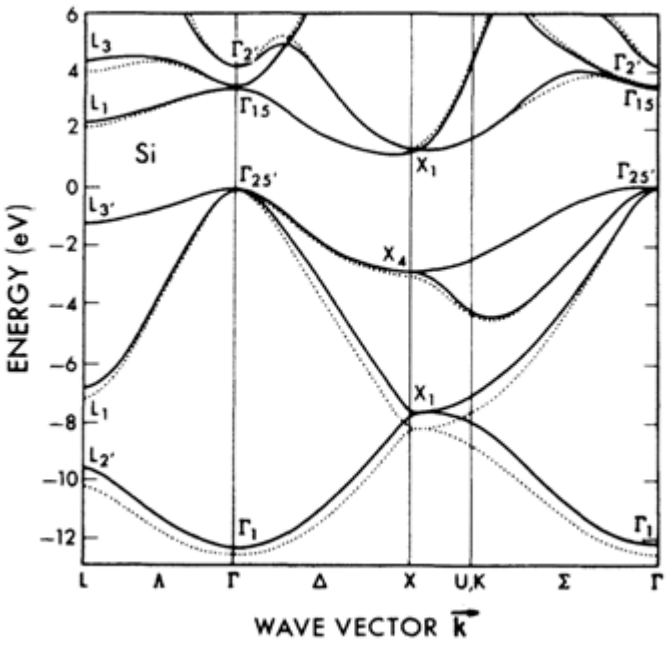

Figure 2.1: Band structure of silicon [20]

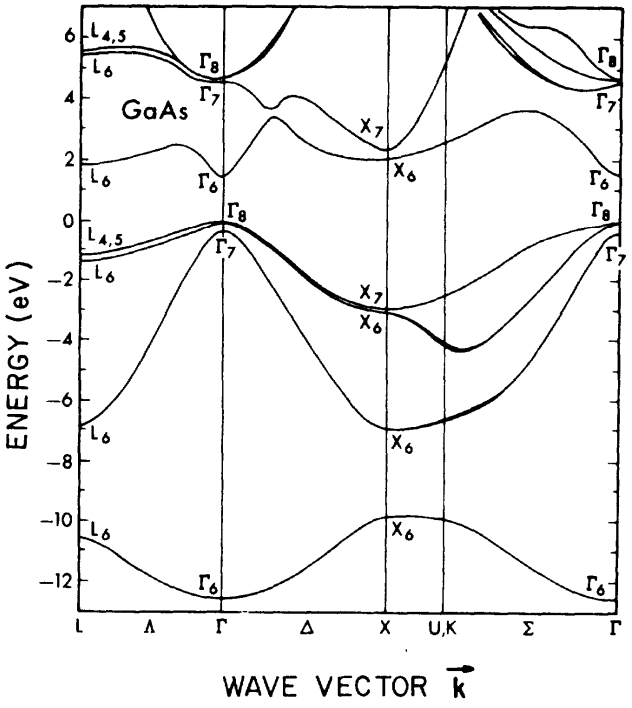

Figure 2.2: Band structure of gallium arsenide [20]

and gallium arsenide (GaAs) (Fig. 2.2). It is interesting to note that the top of the valence band and the bottom of the conduction band do not always occur at the same $\vec{k}$ value. When the top of the valence band and the bottom of the conduction band do occur at the same $\vec{k}$ value this is known as a direct band gap. From Fig. 2.2 one can see this occurs at the centre of the first Brillouin zone (the Γ point) in GaAs. When the top of the valence band and the bottom of the conduction band do not occur at the same $\vec{k}$ value this is known as an indirect band gap. Whether a semiconductor has a direct or indirect band gap is very important to its optical properties, and as we will see is the biggest obstacle in making an efficient silicon light emitter.

2.2 Light Emission from Bulk Semiconductors

Light emission occurs in semiconductors when an electron-hole-pair (EHP) recombines and gives off energy in the form of a photon. This EHP must first be formed by an electron being excited from the valence band up to the conduction band, leaving behind a hole in the valence band. This could happen optically (as in the case of photoluminescence spectroscopy, section 4.2) or electrically (as in an LED). The electron can then fall back down to the valence band and recombine with a hole giving off energy. The exact pathway will depend on whether the band gap is direct or indirect and whether there are any mid-gap defect states. Recombination in both direct and indirect band gap semiconductors is shown in Fig. 2.3.

In a direct band gap semiconductor, the top of the valence band and the bottom of the conduction band occur at the same $\vec{k}$ value (the Γ point). Therefore, while a photon is emitted to conserve energy, the momentum is already conserved because the wave vector

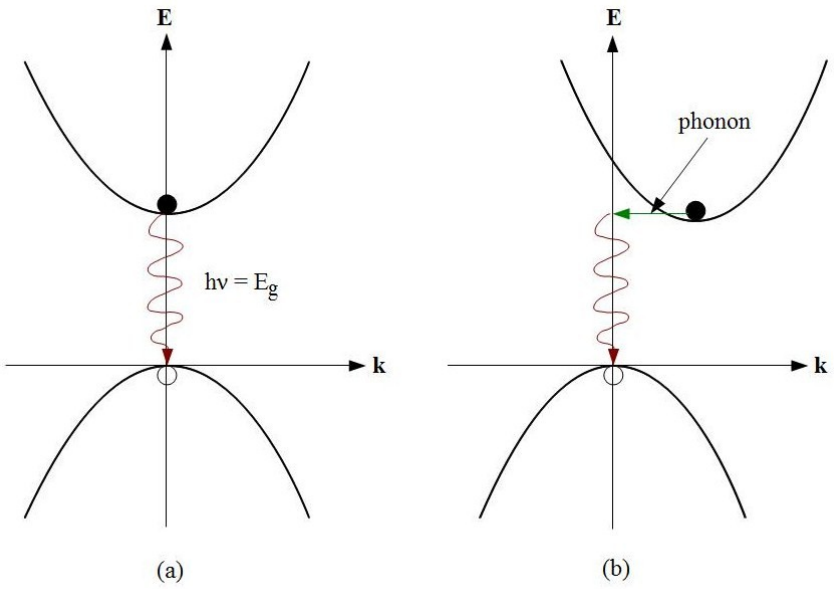

Figure 2.3: Emission from (a) direct and (b) indirect band gap semiconductors

stays the same (the momentum of the photon h/λ is negligible). The minimum energy of the emitted photon, $h\nu$, is simply the difference in the conduction band minimum energy, E_c, and the valence band maximum energy, E_v:

$$h\nu = E_c - E_v = E_g \tag{2.2}$$

where E_g is the band gap energy. Different band gap materials will then emit light at different characteristic wavelengths. This is apparent in the need for different materials for different coloured LEDs, for instance using $GaAs_{1-x}P_x$ with different values of *x*, one can obtain light from red to green, and GaN can be used for blue light [21].

In indirect band gap semiconductors, such as silicon, the wave vector ($\vec{k}$) of an electron changes in a transition from the conduction band to the valence band. Therefore,

for momentum to be conserved, a phonon must also be involved in the interaction. The momentum of the phonon $\hbar\boldsymbol{k}$ must be such that

$$\boldsymbol{k} = \boldsymbol{k}_c - \boldsymbol{k}_v \tag{2.3}$$

where $\boldsymbol{k}_c$ is the wave vector at the conduction band minimum and $\boldsymbol{k}_v$ is the wave vector at the valence band maximum.

The reason why indirect band gap semiconductors are inefficient light emitters can then be explained by observing the internal quantum efficiency. The internal quantum efficiency η_i is given by

$$\eta_i = \frac{\tau_{nr}}{\tau_{nr} + \tau_r} \tag{2.4}$$

where τ_r is the radiative lifetime and τ_{nr} is the nonradiative lifetime [21]. In indirect band gap semiconductors recombination is a three body process involving an electron, a photon and a phonon, which has a low probability of occurring. The radiative lifetime is much longer than the nonradiative lifetime and so the efficiency is very small. Conversely, in direct band gap semiconductors τ_{nr} is much larger than τ_r, so η_i is greater. Values of the radiative and nonradiative lifetimes and internal quantum efficiency for silicon and gallium arsenide are given in Table 2.1 for comparison.

	$\boldsymbol{\tau_r}$	$\boldsymbol{\tau_{nr}}$	$\boldsymbol{\eta_i}$	$\boldsymbol{\tau}$ $(\frac{\mathbf{1}}{\boldsymbol{\tau}} = \frac{\mathbf{1}}{\boldsymbol{\tau_r}} + \frac{\mathbf{1}}{\boldsymbol{\tau_{nr}}})$
Si	10 ms	100 ns	10^{-5}	100 ns
GaAs	100 ns	100 ns	0.5	50 ns

Table 2.1: Lifetimes and internal quantum efficiencies of Si and GaAs [21]

Thus far, it has been assumed that an electron will recombine with a hole directly across the band gap, but it can also do so via a mid-gap state, or trap (shown in Fig. 2.4). This trap could be associated with defects like dangling bonds and dislocations or grain boundaries. The defect state can act as a recombination centre and increase the probability of recombination, which may be radiative or nonradiative [21]. As we will see later, these defect states can be important in silicon nanocluster emission. They are typically due to dangling bonds and surface states at the nanocluster interface.

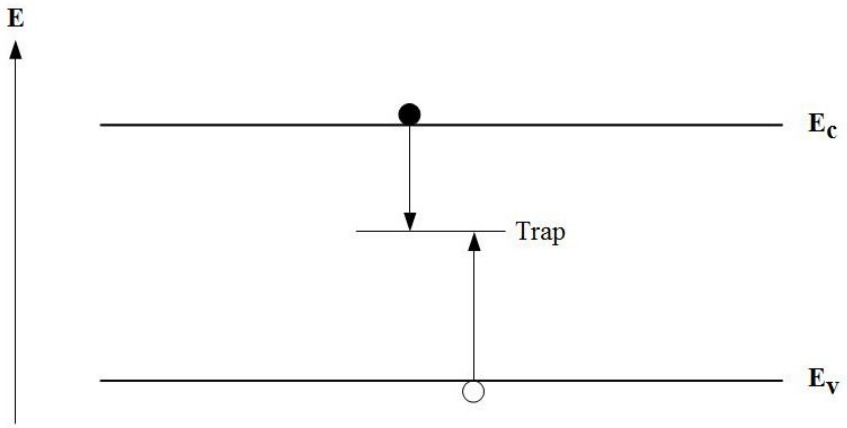

Figure 2.4: Recombination via a trap, or mid-gap state

2.3 Quantum Confinement

It has been stated that indirect band gap semiconductors like silicon, in bulk form, are poor light emitters. However, by reducing the dimensions of the material, quantum mechanical effects can be observed. By spatially confining the electrons and holes, the electronic and vibrational properties are altered, leading to new optical behaviour of the material. Fabrication technology has progressed to the point that most nanostructures can

be produced reliably with high precision, and the goal now is to exploit these novel properties in optical devices.

Typically, the points of reference used for the onset of quantum confinement effects are the de Broglie wavelength and the exciton Bohr radius [21] [22]. The de Broglie wavelength is defined as

$$\lambda = \frac{h}{\boldsymbol{p}} \tag{2.5}$$

where h is Planck's constant and $\boldsymbol{p}$ is the electron's momentum. The Bohr radius is given as

$$a_0 = \frac{4\pi\epsilon_0\epsilon_r\hbar^2}{\mu e^2} \tag{2.6}$$

where ϵ_0 is the permittivity of free space, ϵ_r is the dielectric constant of the material, $\hbar$ is $h/2\pi$, e is the charge of the electron, and μ is the reduced mass of the exciton, defined by

$$\frac{1}{\mu} = \frac{1}{m_e^*} + \frac{1}{m_h^*} \tag{2.7}$$

where m_e^* and m_h^* are the effective masses of the electrons and holes. The de Broglie wavelength and the Bohr radius are typically on the order of nanometres, so the electrons and holes must be confined to areas on the order of nanometres to observe quantum confinement effects.

An electron can be confined in one or more dimensions, resulting in a few different types of nanostructures. If it is confined in one dimension, the structure is known as a quantum well, if it is confined in two dimensions the structure is known as a quantum wire, and if it is confined in all three dimensions the structure is known as a quantum dot.

The effect of quantum confinement can be seen when one observes the change in the electron wavefunction, energy or density of states relative to the bulk case. This change will be different for each of the different nanostructures. For simplicity the quantum well structure will be discussed in detail, though the subsequent results can easily be expanded to the quantum wire and quantum dot scenarios.

In a bulk semiconductor, the electronic wavefunction is of a special form called a Bloch function:

$$\psi_{\boldsymbol{k}}(\boldsymbol{r}) = u_{\boldsymbol{k}}(\boldsymbol{r})exp(i\boldsymbol{k}\cdot\boldsymbol{r}) \tag{2.8}$$

where $u_{\boldsymbol{k}}(\boldsymbol{r})$ has the periodicity of the crystal lattice [23]. Because the electrons are free to move throughout the crystal which has a periodic structure, their wavefunction is a Bloch wave, or a superposition of plane waves. The energy of an electron in is related to the momentum by the equation [21]

$$E = \frac{\hbar^2\boldsymbol{k}^2}{2m_e^*} = \frac{\hbar^2k_x^2}{2m_e^*} + \frac{\hbar^2k_y^2}{2m_e^*} + \frac{\hbar^2k_z^2}{2m_e^*} \tag{2.9}$$

In the quantum well, the electrons are confined in the z-direction so there is a potential barrier in the Schrödinger equation and the wavefunction will differ from the bulk case. Along the z-direction, the wavefunction will look like that of the familiar finite potential well scenario. The wavefunction is no longer a plane wave that is non-zero all throughout space, instead, it is mostly confined to the well because the electron is spatially confined to the potential well.

This shows qualitatively that the form of the wavefunction will change when the electrons are confined, but to obtain some more meaningful information on the

consequences of quantum confinement, one must also look at the change in the energy. The possible values of the wavevector are given by the equation

$$k = \frac{n\pi}{L} \tag{2.10}$$

and so each component of the wavevector follows the same equation

$$k_i = \frac{n_i\pi}{L_i} \quad i = x, y, z \tag{2.11}$$

where n is a positive integer and L_i is the length of the structure in the *i*-direction. It is interesting to note that in the bulk case where the L_i are very large the components of the wavevector have finely spaced values and can be approximated as a continuum. However, in a quantum well where the electrons are confined in the z-direction, $L_z << L_x, L_y$ and $k_z$will take on well separated discrete values. A consequence of this is that the ground state energy is increased relative to the bulk (unconfined) case by an amount ΔE

$$\Delta E = \frac{\hbar^2 k_z^2}{2m_e^*} = \frac{\hbar^2 \pi^2}{2m_e^* L_z^2} \tag{2.12}$$

called the confinement energy [22].

Though this was shown using the quantum well as an example, it can easily be extended to confinement in two directions (quantum wires) and three directions (quantum dots). For a quantum dot, the wavefunction would look like the finite potential well wavefunction in all three directions. The confinement energy would contain the total wavevector ($k_x^2 + k_y^2 + k_z^2$) rather than just the z-component k_z^2 in equation (2.12)

The confinement energy is essentially a manifestation of Heisenberg's uncertainty principle described by

$$\Delta x \Delta p \geq \frac{\hbar}{2} \tag{2.13}$$

When the electrons are confined spatially, the uncertainty in the position (Δx) decreases and consequently the uncertainty in the electrons' momentum (Δp) increases. The increase in the electrons' momentum is the reason for the increase in the ground state energy.

Applying the momentum operator to an eigenstate $\psi_{n\boldsymbol{k}}$ and using equation (2.8) gives

$$\boldsymbol{p}\psi_{n\boldsymbol{k}} = \frac{\hbar}{i}\nabla\psi_{n\boldsymbol{k}} = \hbar\boldsymbol{k}\psi_{n\boldsymbol{k}} + e^{i\boldsymbol{k}\cdot\boldsymbol{r}}\frac{\hbar}{i}\nabla u_{n\boldsymbol{k}}(\boldsymbol{r}) \text{ [16]} \tag{2.14}$$

By this equation the crystal momentum ($\boldsymbol{k}$) is proportional to the electron momentum ($\boldsymbol{p}$), therefore when Δp increases there will be a spread in the wavevector $\boldsymbol{k}$ as well. This results in an overlap of the electron and hole wavefunctions in $\boldsymbol{k}$-space and so the $\boldsymbol{k}$-conservation rule breaks down [24]. Therefore, the spread in the momentum and wavevector allows for optical transitions to occur which do not require a phonon, thereby increasing the efficiency of the emission due to the radiative and nonradiative lifetimes given in Table 2.1.

So far it has been shown that the quantum confinement of electrons will result in an overlap of the electron and hole wavefunctions in $\boldsymbol{k}$-space allowing for recombination without the need of a phonon, thereby increasing the efficiency of emission compared to the bulk case. It is indeed encouraging to know that at least light emission is possible

when the charge carriers are confined; however, one would naturally want a better idea of the nature of the light that will be emitted. It was already stated that quantum confinement will alter the electrons' wavefunction and energy, but a complete theory of the exact nature of these parameters within nanoclusters is needed to better understand the light emission from them.

A theory of the electronic wavefunctions in semiconductor nanoclusters was in fact proposed in 1985 by Brus [25]. It was assumed the luminescence originated from perfectly spherical nanoclusters. As well, though they are not technically excitons, the discrete excited states of these nanoclusters were described as being excitons because of the spatial confinement of the carriers within the nanocluster [26].

The electronic wavefunction in the bulk case is a Bloch function as in (2.8), so the electronic wavefunction in the nanocluster can be approximated as a wave packet of Bloch waves, as it is now localised. If $\Phi_{\boldsymbol{k}}(\boldsymbol{r})$ is a Bloch wave, the electronic wavefunction in a nanocluster can be written as

$$\psi_{k,\mu}(r) = \sum_{\mu} \int_{k} f_{i\mu}(k)\Phi_{k,\mu}(r)dk \tag{2.15}$$

where μ is an index for summation over different bands. Using the Brus model and neglecting higher order terms, the energy of the first excited state is:

$$E = E_g + \frac{\hbar^2\pi^2}{2\mu r^2} - \frac{1.8e^2}{4\pi\epsilon_o\epsilon_r r} \tag{2.16}$$

The second term accounts for the widening of the band gap due to the spatial confinement of the carriers within the nanocluster. The third term accounts for the decrease in energy due to the Coulombic interaction of the electron and hole.

This energy of the first excited state of the exciton in (2.16) can also be thought of as the band gap energy within the nanocluster. Therefore the band gap energy of the nanocluster depends on its radius, the smaller a nanocluster is, the larger its band gap. As the radius of the nanocluster increases, the band gap energy decreases until it is the same as the bulk silicon band gap energy of 1.1 eV.

Theoretical work on light emitting quantum confined structures like in the preceding discussion has been ongoing for several decades, though the first experimental evidence of quantum confinement of silicon was only made in 1990 by Canham using porous silicon [13]. The porous silicon was fabricated by chemical dissolution of silicon wafers in concentrated (40%) aqueous HF. The silicon is etched away leaving columnar pores surrounded by the silicon matrix. By extending the amount of time in HF, the widths of the columns grow, increasing the porosity until they reach the neighbouring columns and the microscopic structure is that of isolated silicon columns. When the widths of these columns are less than the Bohr radius (2.6), quantum confinement effects can be observed.

For the most part, the luminescence of porous silicon can be explained by quantum confinement [13] [27]. For instance, the emission energy is shifted to higher energies at higher porosity (smaller column widths). However, certain aspects of the emission are not completely explained by the Brus model. This is because the Brus model neglects an important characteristic of porous silicon and nanocluster emission: the effect of surface states and/or states at the nanocluster-matrix interface, as well as defect states.

The role of surface states in porous silicon luminescence has been investigated by Wolkin *et al.* [28]. The photoluminescence (PL) of porous silicon samples with varying porosities was observed to span the visible spectrum when under vacuum. After exposure to air, a redshift in the PL was observed, as large as 1 eV. This redshift was attributed to the trapping of an electron or exciton by Si=O bonds on the surface, which produce localized levels in the band gap of nanoclusters smaller than about 3 nm. Fig. 2.5 shows the calculated electronic states in silicon nanoclusters as a function of cluster size and surface passivation. Though the band gap continues to increase at smaller cluster sizes, the trapped electrons in Zone II and trapped excitons in Zone III introduce mid-gap states, allowing for lower energy emission between these states rather than across the band gap

After the first experimental evidence of quantum confinement in silicon was found using porous silicon, there was an enormous amount of interest in the luminescence characteristics of this material [29]. However, it is not the only way to achieve silicon nanostructures capable of efficiently emitting light. In fact, the present work exclusively deals with another method of creating silicon nanostructures, namely embedding silicon nanoclusters, or quantum dots, in a dielectric matrix.

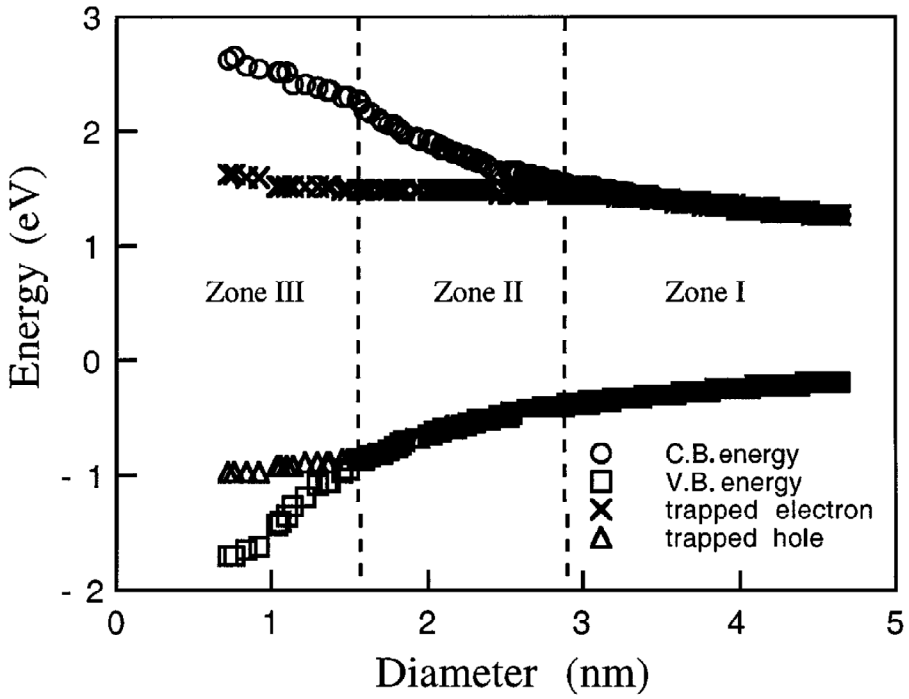

Figure 2.5: Oxygen passivation introduces mid-gap states as the size of the silicon nanoclusters decreases [28]

2.4 Silicon Nanocluster Embedded Dielectrics

Typically, silicon nanoclusters are formed in a silicon dielectric, either silicon oxide or silicon nitride, by a thermal anneal of a silicon rich film. The anneal promotes phase separation between the dielectric and the excess silicon, which accumulates to form the nanoclusters, as shown in Fig. 2.6. This silicon rich film can be formed in a number of ways, including chemical vapour deposition, ion implantation and sputtering [30].

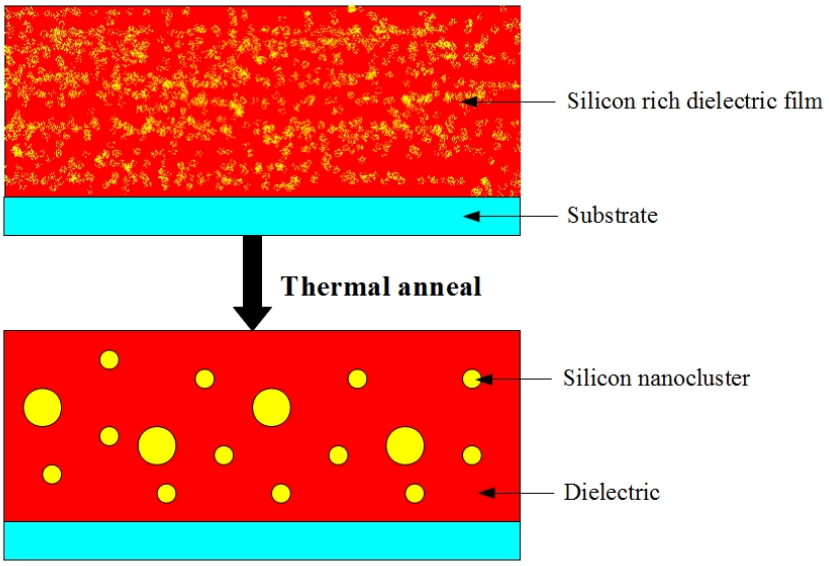

Figure 2.6: Silicon nanoclusters formed by annealing a silicon rich dielectric

Silicon oxide was initially the dielectric of choice and most of the literature in the field pertains to nanoclusters embedded in silicon oxide. The luminescence from these films is quite varied and sensitive to the fabrication processes. There has been much debate over the origins of the luminescence, whether it is from the quantum confinement of the silicon nanoclusters, surface states at the nanocluster-matrix interface, or defect states in the matrix. For instance, Komoda *et al.* [31] observed luminescence in the 600-800 nm range while Mutti *et al.* [32] observed luminescence in the 490-540 nm range, yet they both attributed the luminescence peaks to quantum confinement effects. For both studies, the dependence of the emission energy on annealing temperature agreed with the Brus theory and TEM images confirmed the presence of silicon nanocrystals. However,

Liao *et al*, [33] observed emission around 460 nm and determined it to be from oxygen vacancies in the film.

There have also been studies showing multiple PL peaks, and both defect states and quantum confinement have been credited with contributing to the luminescence in these films. For instance, Shimizu-Iwayama *et al.* [14] observed visible photoluminescence with peaks around 2.0 eV (~620 nm) and 1.7 eV (~730 nm). The 620 nm band was present in as-implanted samples but disappeared after annealing at 500^{o}C and was attributed to so-called *E'* centre defects. The 730 nm band appeared after annealing at 1100^{o}C and was attributed to the formation of silicon nanoclusters in the silicon oxide. Another example showing this is a study by Wen *et al.* [34]. The PL observed contained two broad peaks with comparable intensities at low temperature. The peak located at 600-850 nm was attributed to the quantum confinement effect, whereas the peak located at 450-600 nm was attributed to defect states of the silicon oxide.

A comprehensive study of the PL evolution of silicon-implanted SiO_2 was performed by Song & Bao [35]. They found four different bands in the PL spectra, shown in Fig. 2.7. When the samples were annealed in N_2 at a temperature below 1000^{o}C the spectrum consisted of three bands, centred at about 470, 550, and 630 nm. After annealing above 1000^{o}C for a long enough time, the three previous bands disappeared and there emerged one peak centred around 730 nm. Using electron paramagnetic resonance (EPR), the as-implanted sample was found to have a resonance for the *E'* centre defect ($O_3{\equiv} Si{\cdot}\ \cdots^{+}Si{\equiv} O_3$ or ${\cdot}Si{\equiv} O_3$) shown in Fig. 2.8. However, the number of *E'* centre defects decreased with annealing time and temperature and it was identified as a

nonradiative recombination centre, disagreeing with [14]. Instead, Song & Bao attribute the 630 nm band to another radiative defect called the nonbridging oxygen hole centre (NBOHC).

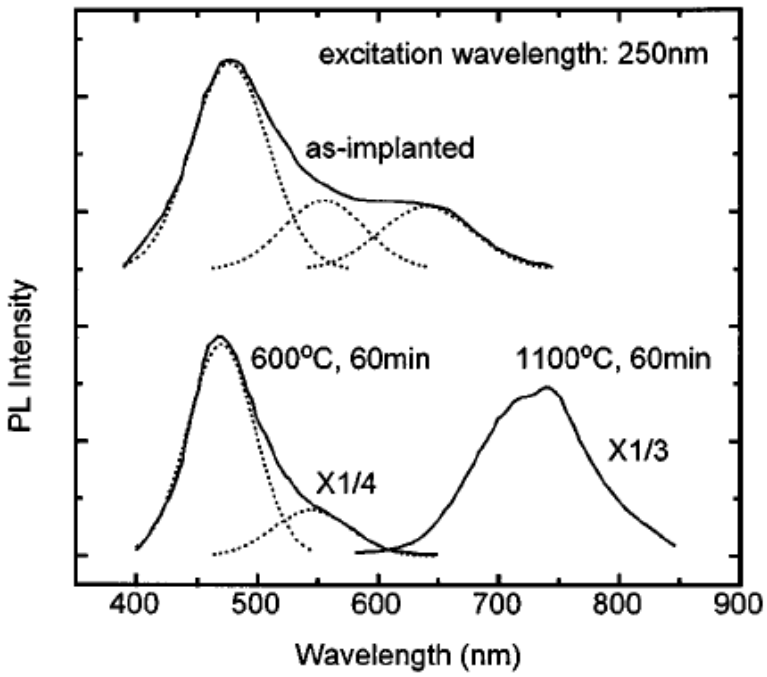

Figure 2.7: Four different PL bands from silicon-implanted SiO_2 [35]

One can see from Fig. 2.8 that another defect centre was observed with EPR, the *D* centre ($(\cdot Si\equiv Si_3)_n$). The number of *D* centres remained relatively constant with annealing and is evidence of silicon clustering. The silicon nanoclusters are amorphous until annealed above 1000°C, at which temperature they crystallize. This can be seen in the x-ray photoelectron spectroscopy (XPS) spectra shown in Fig. 2.9, where the 99.4 eV peak for crystal silicon only appears after annealing above 1000°C. The 730 nm PL band is correlated with this crystallization of the silicon nanoclusters and the disappearance of

defects. However, since the band does not exhibit a red shift at higher anneal temperatures, the luminescence was explained to be coming from surface states at the nanocrystal-matrix interface.

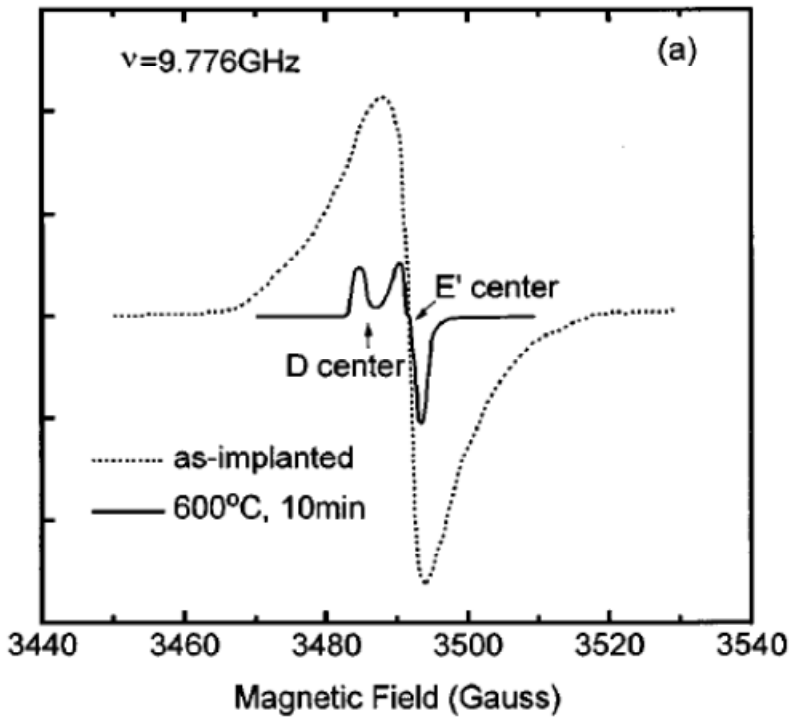

Figure 2.8: EPR spectrum showing the *E'* and D centre defects [35]

The 470 nm PL band was attributed to oxygen vacancies, agreeing with Liao *et al.* [33] and Nishikawa *et al.* [36]. The 550 band was attributed to another defect state, the exact nature of which, however, was not known.

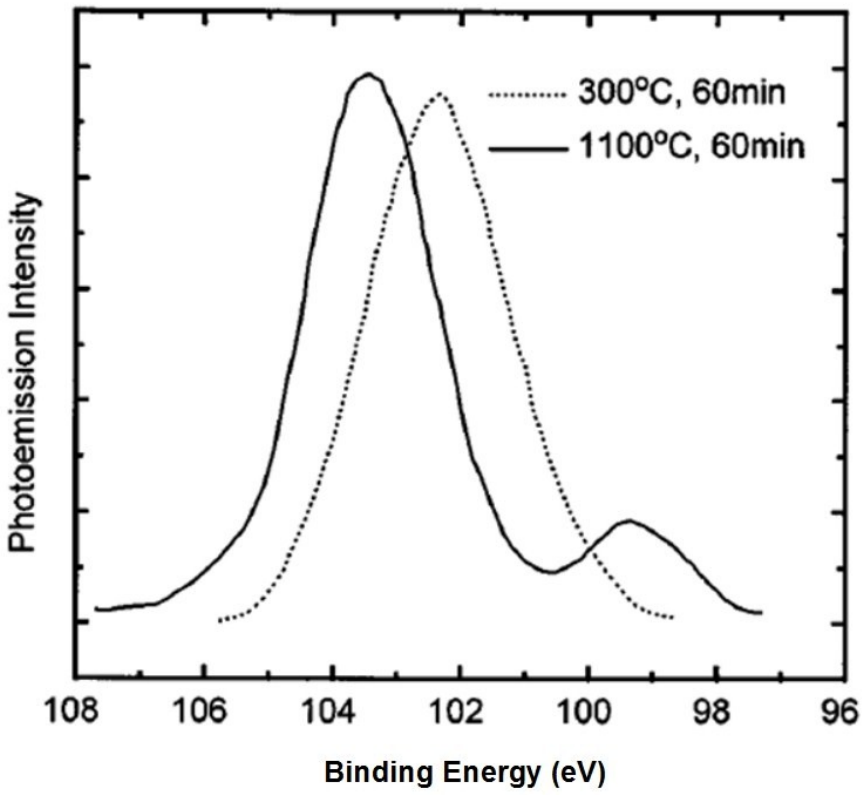

Figure 2.9: XPS spectra showing the crystalline silicon peak (99.4 eV) appearing after a 1100°C anneal [35]

A study by Iacono *et al.* [37] showed that amorphous silicon nanoclusters were formed in SiO_2. However, the formation of these nanoclusters did not occur until after annealing above 1000°C, agreeing with [35]. Fig. 2.10 shows energy filtered transmission electron microscopy (EFTEM) and conventional dark field TEM (DFTEM) images of the films annealed at 1150°C and 1250°C. The DFTEM images only show crystalline nanoclusters, which are only apparent after annealing above 1000°C, whereas the EFTEM images are able to show amorphous nanoclusters as well.

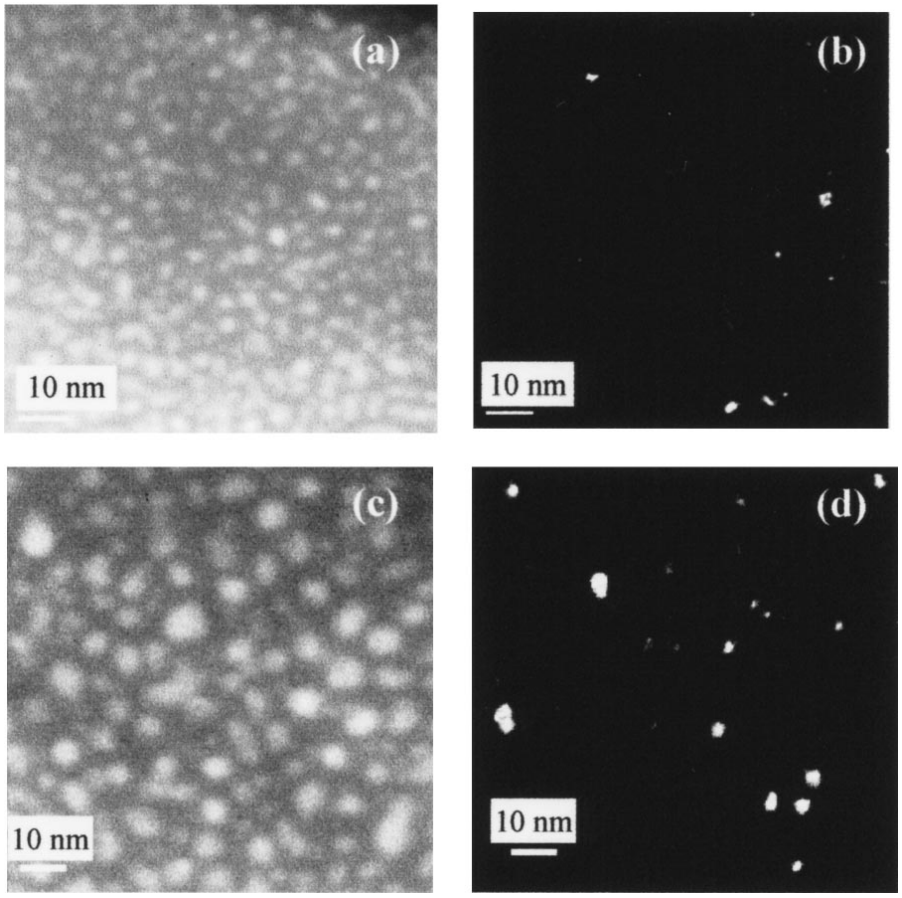

Figure 2.10: EFTEM images of SiO_x films annealed at (a) 1150°C and (c) 1250°C. DFTEM images of SiO_x films annealed at (b) 1150°C and (d) 1250°C [37]

In summary, it has been shown that silicon nanoclusters do form in silicon oxide, though they do not crystallize until annealing above 1000°C. Several PL bands have been observed; the exact nature of this luminescence is still under debate and has been attributed to both quantum confinement and defect states, though defect states seem to play a more prominent role.

As mentioned in section 1.1, luminescence from silicon rich silicon nitride (SRSN) films has gained interest in recent years. In this system, besides quantum confinement, luminescence can again come from defect states in the matrix, though they

are different than the silicon oxide defect states. Deshpande *et al.* [38] proposed a model for the defect states in silicon nitride which relies on four sources of the defect emission: Si-Si bonds, N-N bonds, and Si and N dangling bond. A schematic of this model is shown in Fig. 2.11. The three PL peaks of their hot filament-assisted CVD films can be explained by their model. A broad 2.5 eV (~495 nm) peak is due to recombination at the silicon dangling bonds (K^0 centre). A 3.0 eV (~415 nm) peak is due to recombination between either the conduction band and the N_2^0 level, or the valence band and the N_4^+ level. Finally, a 1.8 eV (~690 nm) peak is due to the recombination between the N_4^+ and N_2^0 levels.

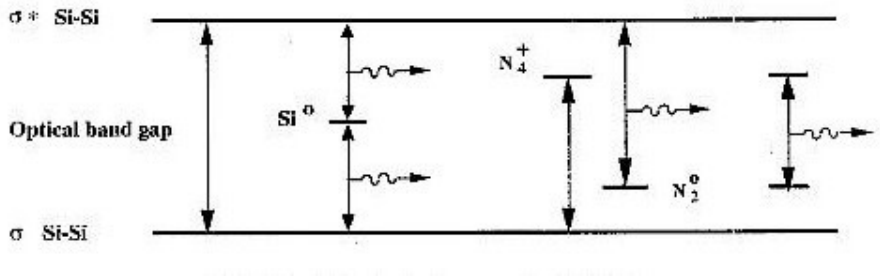

Figure 2.11: Model for the defect states in silicon nitride [38]

One problem with silicon rich silicon oxide (SRSO) films is that the emission from the silicon nanoclusters only reaches as far as the near-infrared range, even when the size of the clusters were controlled to below 2 nm [39]. Any observed visible luminescence was generally attributed to defects which disappeared after either a high temperature anneal or hydrogen passivation [35] [40]. It has been demonstrated that though both SRSO and SRSN display PL peaks after high temperature annealing due to silicon nanocluster formation, the peak positions from nitride passivated films are

blueshifted by about 0.6 eV so that its luminescence is in the visible range [41]. The reason for this blueshift was explained by the fact that the presence of nitrogen results in lower strain at the silicon-dielectric interface than with oxygen, leading to less of a reduction of the silicon nanocluster band gap. This finding is encouraging in that it suggests by using silicon nitride as the host matrix, a device may possibly be made in which the emission wavelength can be tuned across the visible range by controlling the size of the nanoclusters.

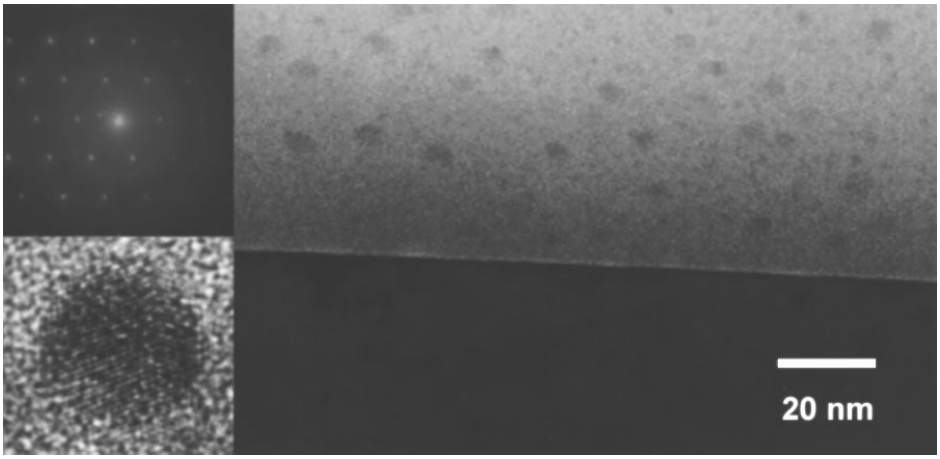

Figure 2.12: TEM images showing the presence of crystalline silicon nanoclusters in a silicon nitride film [42]

Indeed, it has been shown that the PL spectra from SRSN can be tuned across the visible range by varying the nanocluster size. Kim *et al.* [42] observed silicon nanocrystals embedded in silicon nitride by TEM, shown in Fig. 2.12. By varying the size of the nanocrystals, PL emission was tuned from the near-infrared (~900 nm) to the ultraviolet (~400 nm), shown in Fig. 2.13. As well, Park *et al.* [16] observed amorphous silicon nanoclusters in silicon nitride with TEM. By varying the size of these nanoclusters, the PL emission was tuned from approximately 450 nm to 620 nm.

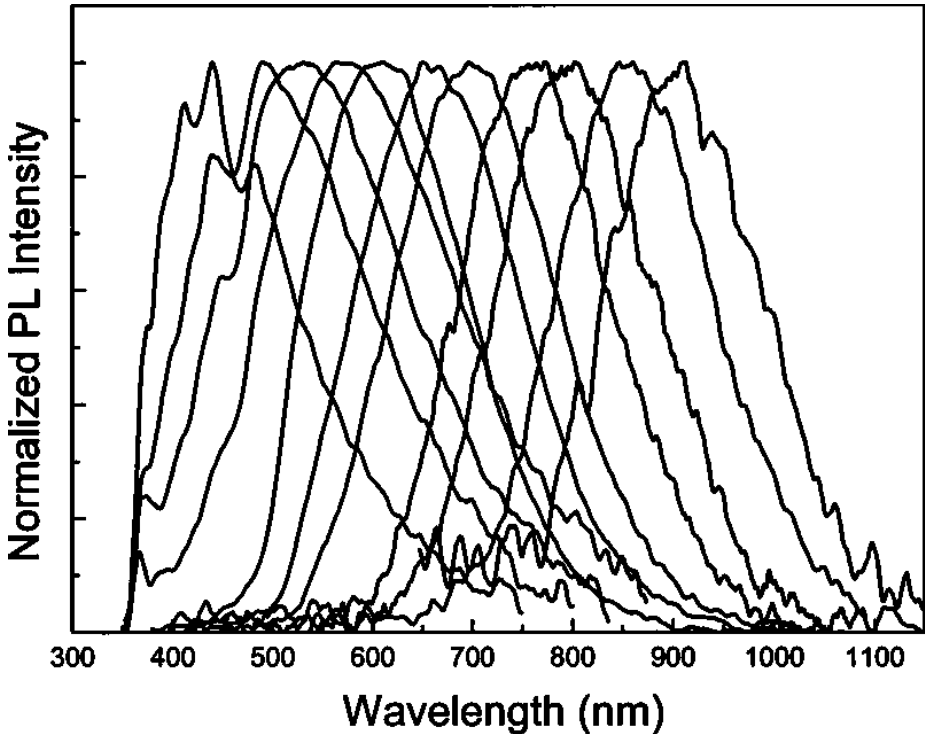

Figure 2.13: PL emission can be tuned across the visible range by varying the size of the nanoclusters [42]

Though these authors attributed the luminescence of their SRSN films to quantum confinement effects in the silicon nanoclusters, others have claimed it to be due to defect and interface states. Dal Negro *et al.* [43] and Bregolin *et al.* [44] attributed the emission from their SRSN films to nitrogen-related defect states at the nanocluster-matrix interface. Both observed similar PL spectra which appeared to be comprised of three bands, centred around 750, 900-950, and 1050-1100 nm. However, the shape and position of the spectra did not change with differing excess silicon concentration or with annealing temperature. In addition, when investigating the temperature dependence of the PL, it was observed that it did not follow a bell-shape behaviour centred about 100 K like the luminescence from silicon nanocrystals embedded in silicon oxide [45]. Instead, the

behaviour was more accurately described by the thermal ionization of local radiative traps. For these reasons, these authors attributed the luminescence to nanocluster-matrix interface states.

Wang *et al.* [46] observed luminescence from both silicon nanoclusters and defect states in their SRSN films. With 514.5 nm excitation the 1100^{o}C annealed films emitted red light due to the quantum confinement effect in the silicon nanoclusters. However, with 325 nm excitation, luminescence from silicon and nitrogen dangling bonds was observed in both the as-deposited and 1100^{o}C annealed films. Therefore, both nanoclusters and dangling bonds were present in the annealed samples, but which emission centre was excited depended on the excitation energy. The 325 nm excitation is enough to excite both the nanoclusters and the defects; however, because of the much shorter radiative lifetime of the defect centres and the comparatively weak PL emission from the nanoclusters, the emission at that excitation energy was almost solely from defect states. The 514.5 nm excitation is not a high enough energy to excite the defects, so only the PL from the nanoclusters was seen at that excitation energy.

It is interesting to note that the dangling bond defect states in the silicon films do not disappear with high temperature annealing like the defect states in silicon oxide films. However, after hydrogen passivation the defect emission can be suppressed as the dangling bonds are bonded to hydrogen atoms. As well, the nanocluster emission is enhanced as there is a lower interface trap density, increasing the charge retention in the nanoclusters [47] [48].

Besides the many studies of PL in these films, electroluminescence (EL) has also been observed in SRSO [49], SRSN [17], and silicon rich oxynitride (SRON) films [50]. In addition to this, with recent discovery of optical gain in silicon nanocrystals [15], there is considerable evidence that a silicon-based laser or LED may well soon be a reality.

2.5 Rare Earth Doped Dielectrics

An interesting characteristic of silicon nanostructures is the possibility to transfer energy to rare earth ions within the same host matrix [18] [51]. Silicon nanocluster emission generally exhibits a fairly broad spectrum, but energy can be transferred to rare earth ions to obtain a specific emission energy, which will depend on which element is used as the dopant. There are several rare earth ions which can be used to obtain emission in the visible and infrared range (e.g. Ce, Tb, Er), but this work has only made use of cerium implanted into stoichiometric and silicon rich silicon nitride films.

Rare earths have been used in phosphors in CRT displays for decades. These phosphors were able to exploit the visible transitions of the Eu^{3+}, Tb^{3+}, and Ce^{3+} ions, producing red, green, and blue light. In recent decades, Er^{3+} has gained considerable interest due to its emission wavelength around 1530 nm (the energy levels of Er^{3+} are shown in Fig. 2.14), corresponding to the low attenuation region of silica optical fibres [52]. The transition responsible for this luminescence occurs within the partially filled 4*f* shell and has a very low absorption cross section [53]. However, a strong coupling between the silicon nanoclusters and Er^{3+} ions has been demonstrated. The absorption cross section of silicon nanoclusters is much higher than that of erbium, so nanoclusters

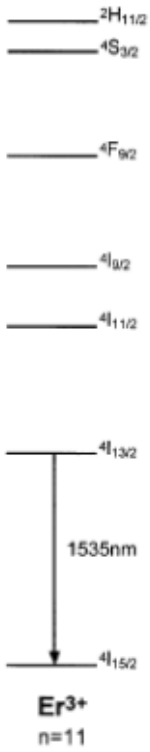

Figure 2.14: An example of the energy level scheme for a rare earth element. The primary emission from Ce^{3+} is ~450 nm [18]

can be used to absorb energy and then transfer it to the erbium ions. Because of this, the effective erbium absorption cross section in SRSO films is up to four orders of magnitude greater than the Er^{3+} optical absorption cross section in silica at a pump wavelength of 488 nm [52]. As a result, the PL intensity of the 1530 nm peak in SRSO has been shown to be approximately ten times the intensity in SiO_2 [54].

In addition to erbium's application in telecommunications, rare earth dopants that emit in the visible range could be used to fabricate silicon based devices for displays or solid-state lighting. The one dopant in particular used in this work was cerium. The emission from Ce^{3+} ions corresponds to $5d \rightarrow 4f$ transitions and is UV/blue light around

400-450 nm. The transition is from the lowest energy 5*d* state to one of the lower energy 4*f* states, $^2F_{7/2}$ and $^2F_{5/2}$, resulting in two closely overlapping PL bands [55]. As a free ion, the five 5*d* orbitals in Ce^{3+} are divided into two energy levels. When embedded in a solid however, the degenerate energy levels are split and the position of the lowest energy 5*d* state depends on the surrounding environment [56].

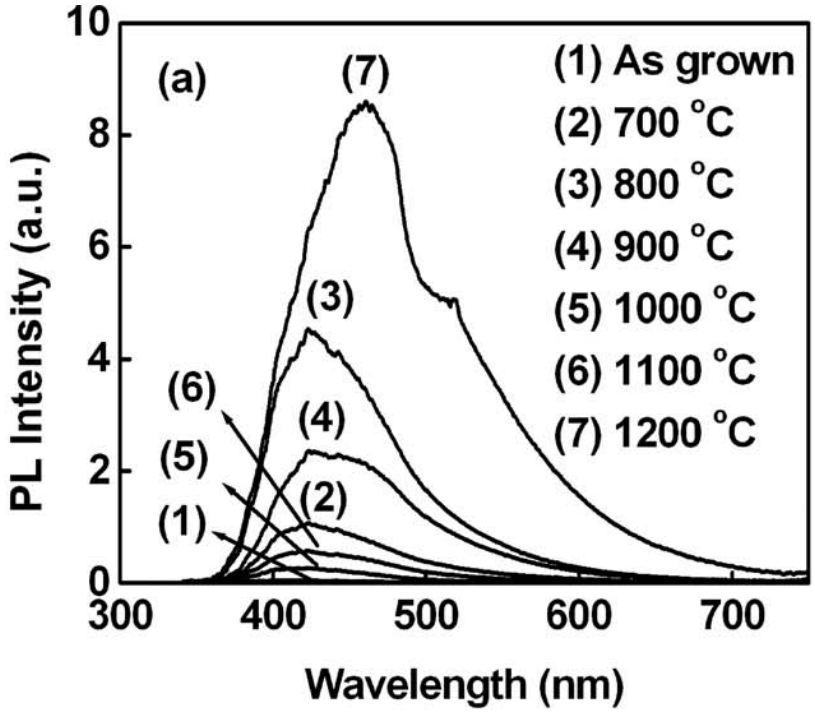

Figure 2.15: PL spectra of Ce-doped SiO_x films [55]

Some work has been done on cerium-doped silicon oxides [55]. The cerium-doped silicon oxide films with cerium concentrations up to 0.9 atomic percent were annealed between 700°C and 1200°C. The PL spectra from a sample with 0.9 atomic percent of Ce are shown in Fig. 2.15. The as-deposited samples do not exhibit any luminescence, as in the precursor phase cerium exists as the optically inactive tetravalent ion Ce^{4+}. With

annealing, the Ce^{4+} ions are converted to the optically active Ce^{3+} ions. Luminescence from the Ce^{3+} ions can be seen in Fig. 2.15 at the anneal temperatures 700-1100°C, with the maximum being at 800°C. After annealing at 1200°C, there is a drastic increase in the PL intensity attributed to the formation of cerium silicate, the presence of which was confirmed by transmission electron microscopy (TEM). In addition, the intensity can be further increased by increasing the anneal time from 1 hour to 3 hours (Fig. 2.16).

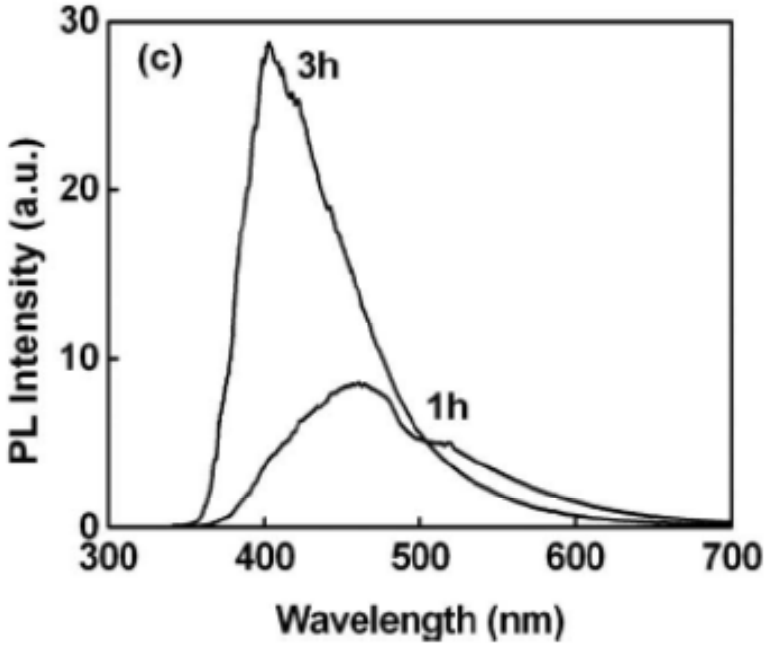

Figure 2.16: The cerium emission increased with a longer anneal [55]

There are few reports on cerium-doped silicon nitrides, so the objective of the rare earth doping part of this work was to investigate those materials in particular and see how they compare to doped silicon oxides. Though nanocluster emission is too low in energy to excite the cerium ions as is done with erbium ions, the role silicon nanoclusters can

play in cerium emission was investigated by doping cerium into SRSN, in addition to stoichiometric silicon nitride.

Chapter 3: Fabrication of Silicon Nitride Films

As discussed in Section 2.4, silicon nanoclusters are formed in a silicon-based dielectric by thermal annealing of a silicon rich film. The anneal promotes phase separation between the excess silicon and the dielectric matrix as the heat provides enough energy for the excess silicon to nucleate and form nanoclusters. Most previous work on silicon nanocluster-embedded dielectrics have centred on using silicon oxide as the host matrix, however, silicon nitride has the advantage of a lower band gap providing less of a barrier for carrier injection. This work has exclusively used silicon nitride as the host matrix for the silicon nanoclusters. Besides changing the host dielectric, a couple of other changes to the standard fabrication process previously used in our group were made as well.

Previous work in our group had silicon rich silicon oxide (SRSO) or silicon rich silicon nitride (SRSN) films produced by chemical vapour deposition, where adjusting the gas flow rates can alter the relative concentrations of the elements in the film [57] [58]. In contrast, the films used in this research were made by first depositing a stoichiometric silicon nitride (Si_3N_4) film, then using an ion implanter to introduce the excess silicon. One advantage of this technique is that implantation of the excess silicon allows for the concentration and depth of the implanted ions to be very carefully controlled, allowing for more control of nanocluster size, concentration and location [59]. In addition, ion

implantation is a technique commonly used in industry and is compatible with VLSI processing technology [60].

There are two reasons for an annealing treatment after ion implantation. As is the case with deposited silicon rich films, the heat treatment is needed for the excess silicon to nucleate and form nanoclusters as well as activate radiative defects [61]. However, when using an implanter, an anneal is also needed to repair radiation damage from the ion beam [62].

The anneal step in the process was also different than a lot of previous work in the field. Rather than using a tube furnace, a rapid thermal processor was used. Besides drastically cutting down on the time required for the anneal, an advantage of this approach is that rapid thermal processing is a commonly used technique in CMOS processing [63].

This chapter will discuss the different instruments that were used in the preparation of the silicon rich silicon nitride films: chemical vapour deposition (CVD), ion implantation, and rapid thermal annealing (RTA).

3.1 Chemical Vapour Deposition

Out of the many methods for depositing thin films, the one most often used to deposit a dielectric like SiO_2 or Si_3N_4 is chemical vapour deposition (CVD). In CVD, source gases chemically react in a chamber, resulting in a film being deposited atomistically on a suitable substrate [64]. The steps involved in CVD are shown in Fig. 3.1.

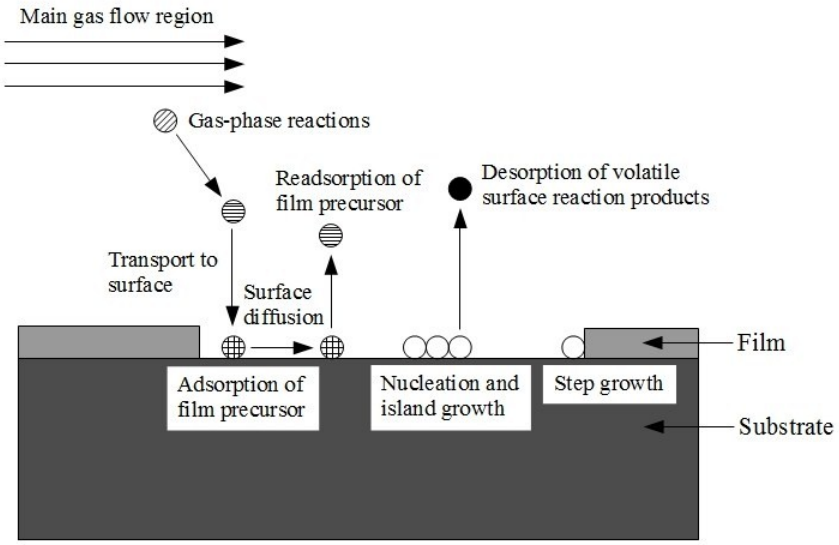

Figure 3.1: The steps involved in the CVD process. After [64]

The gas molecules of the source gases enter the reaction chamber where they undergo chemical reactions in the gas phase to produce new reactive species. These reactants and products are transported to the substrate where the adsorption and diffusion of these species along the substrate surface takes place. Reactions on the substrate surface lead to film formation and the volatile by-products of these reactions are desorbed from the surface and transported out of the chamber [64]. There are different types of CVD but these general steps apply to all of them,

Two different types of CVD were employed to deposit the silicon nitride films: inductively coupled plasma chemical vapour deposition (ICP-CVD) and low pressure chemical vapour deposition (LPCVD).

3.1.1 Inductively Coupled Plasma Chemical Vapour Deposition

Dielectric films like SiO_2 and Si_3N_4 have traditionally been deposited by low pressure chemical vapour deposition (LPCVD) above 700^{o}C, but these temperatures are too high for current VLSI processes [65]. There seems to be a trade off because to be compatible with large scale integrated circuit techniques the dielectric films must be deposited at a lower temperature, but if the temperature is too low, there will not be sufficient energy for the chemical reactions to occur. Fortunately, a method called plasma-enhanced chemical vapour deposition (PECVD) allows for low temperature (<400^{o}C) deposition of silicon nitride films. This is achieved by the plasma transferring enough energy to the gas molecules for the necessary chemical reactions to take place, even at a lower temperature [64].

Plasmas have been generated and studied for over a century, but a key development in the use of plasmas for film deposition was in 1962, when Anderson presented a novel method for sputtering dielectric films in a plasma [66]. This plasma was created by applying an RF field inside a glass tube. Modern processing plasmas have much stricter requirements, such as a high plasma density and good uniformity over large areas. Over the past decades different plasma sources like electron cyclotron resonance (ECR) plasmas, helicon wave plasmas and inductively coupled plasmas (ICP) have been developed and improved to meet these requirements [67]. In this work, an inductively coupled plasma chemical vapour deposition (ICP-CVD) system was used.

In general, an ICP is created by having an inductive element (for instance, a solenoidal coil) inside or around a chamber containing a gas. An RF signal through the

coil creates a time-varying magnetic flux, which by Faraday's Law induces an RF electric field. This electric field accelerates the electrons in the atoms, thereby ionizing the gas and creating the plasma [67].

A schematic of the ICP-CVD system at McMaster is shown in Fig. 3.2. A detailed explanation of this system will not be given here, but can be found in H. Zhang's M.A.Sc. thesis [68].

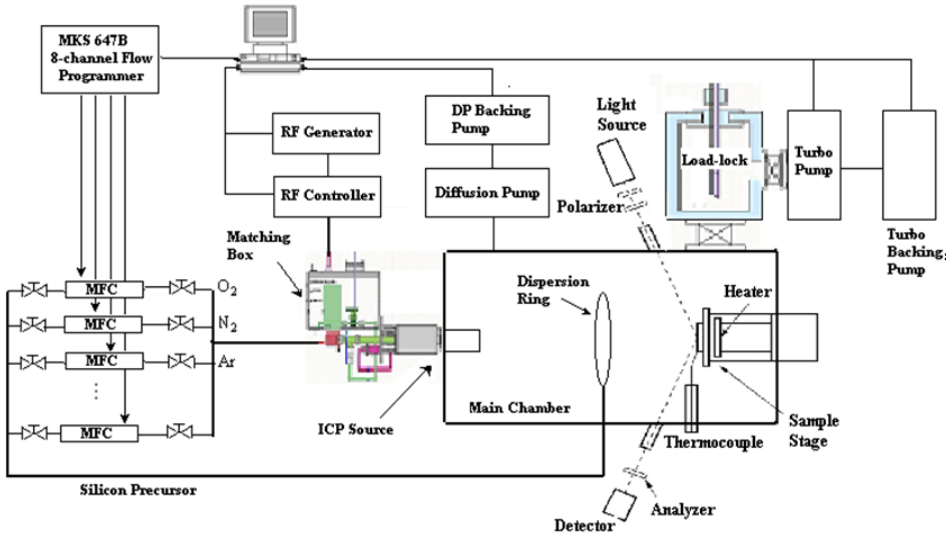

Figure 3.2: The ICP-CVD system at McMaster University

The silicon source gas used was silane (30% SiH_4 in Ar), and pure N_2 was used as the nitrogen source. A pure Ar source was used as the plasma gas. There are additional sources containing pure O_2, an O_2 mixture (10% O_2 in Ar) and a N_2 mixture (10% N_2 in Ar), but these were never used.

The depositions were never used to create SRSN films but rather stoichiometric Si_3N_4 films. Therefore, the parameters remained the same for all depositions to obtain

consistent results. The chamber pressure was kept around $2x10^{-8}$ Torr, the substrate stage was heated to a temperature of 350°C, and an RF power of 300 W was used. For all depositions the flow rates were 5 sccm for SiH_4, 10 sccm for Ar and 10 sccm for N_2.

One parameter that was changed, however, was how the N_2 was introduced. The N_2 can be introduced into the main chamber either by a dispersion ring, or through the plasma. The difference between films deposited in these ways will be addressed in detail in the results section of this thesis.

The progress of the depositions was monitored *in-situ* with a J. A. Woollam spectroscopic ellipsometer which operates in the range of 600 to 1100 nm. This can be used to measure the thickness and refractive index of the films during deposition. Post deposition the refractive indices were measured with a Philips PZ2000 ellipsometer operating at 632.6 nm. The refractive indices for the dispersion ring and plasma samples were measured to be 1.92 and 1.75 respectively.

3.1.2 Low Pressure Chemical Vapour Deposition

Films were also deposited at Carleton University in Ottawa using LPCVD to compare with the films deposited on the ICP-CVD system at McMaster. LPCVD is done at a lower pressure than the simplest CVD process, atmospheric pressure chemical vapour deposition (APCVD), typically around 1 torr. This increases the diffusion compared to APCVD and also forces the temperature to be increased [1]. The films were made with a mixture of flowing NH_3 and Cl_2SiH_4 gases, the temperature at 820°C, and the final thickness was measured as 50±2 nm.

3.2 Ion Implantation

Ion implantation is a key method of impurity doping of semiconductors along with diffusion. It is a commonly used technique in industry, though typically it is donor or acceptor atoms being implanted to make the semiconductor n or p-type. In this work, silicon ions (Si^+) were implanted into stoichiometric silicon nitride (Si_3N_4) films to provide excess silicon for nanocluster formation. This allows for more precise control over the concentration of excess silicon, though rather than being uniform throughout the film as in CVD, the silicon ions will be implanted in a Gaussian distribution [69].

A schematic of a general ion implanter is shown in Fig. 3.3. There are a few different types of ion sources, but a very common one, and the one that is used in McMaster's implanter, is a hot cathode arc source. A heated tungsten filament (the cathode) emits electrons which then ionize the source gas present creating a plasma [62]. The positive ions are extracted through a small aperture and sent into a magnetic field perpendicular to the direction of propagation of the beam. The ions will be subjected to a Lorentz force and deflected, lighter ions being deflected more than heavier ones. By adjusting the magnetic field, ions of a particular mass can be selected and sent through another aperture to the accelerator tube.

In the accelerator tube the ions are subjected to an electric field, accelerating them across a voltage in the kV to MV range. At the end of the accelerator tube the ions enter the process chamber and hit the target wafer. Beam scanning must be used to achieve uniform exposure of the implantation profile. This is accomplished by one of two methods: mechanical scanning and electrostatic scanning. The implanter at McMaster

uses electrostatic scanning, which utilizes scanning plates at different potentials to change the direction of the ion beam.

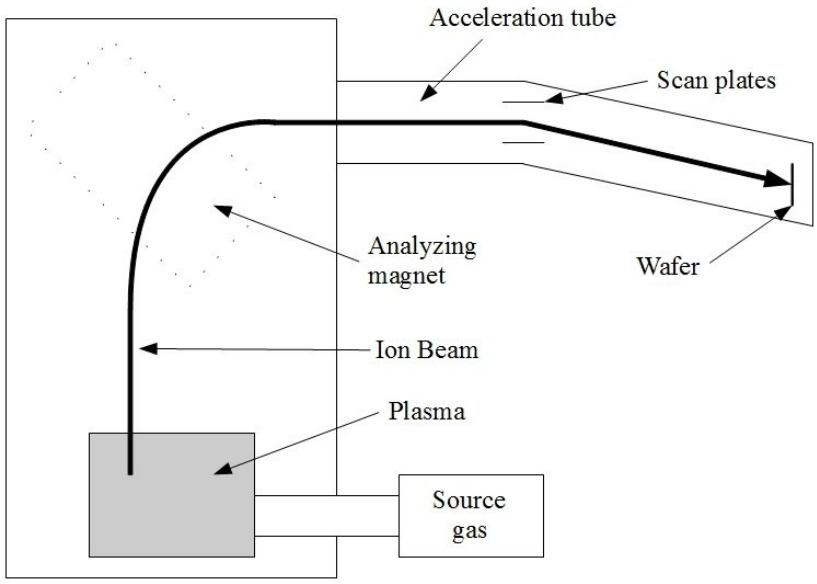

Figure 3.3: Schematic of a general ion implanter

To determine an appropriate excess silicon concentration for maximum light emission, samples were first implanted with fluences of silicon ions ranging from 8.0×10^{15} cm^{-2} to 1.0×10^{17} cm^{-2}. This resulted in maximum light emission around a fluence of 4.5×10^{16} cm^{-2}, and later samples were made with this concentration. SRIM software was used to estimate the expected depth profile of the implanted ions and determine an appropriate accelerating voltage. Silicon ions were implanted at 40 keV except for the later 4.5×10^{16} cm^{-2} samples which were done at 30 keV. The cerium ions were also implanted at 30 keV.

3.3 Rapid Thermal Annealing

After the films had been deposited and implanted with excess silicon, they needed to be annealed to form the silicon nanoclusters, activate any radiative defects, and repair damage from the ion beam. Rather than using a tube furnace where the anneals are generally around an hour long, rapid thermal annealing (RTA) was used because it is a commonly used technique in CMOS processing [63], it greatly reduces the time needed for annealing if used on its own, and if done prior to a conventional furnace anneal it has been shown to strongly enhance luminescence [70]. The annealing step was done using a Jipelec JetFirst 100 Rapid Thermal Processor (RTP). A schematic of the RTP is shown in Fig. 3.4.

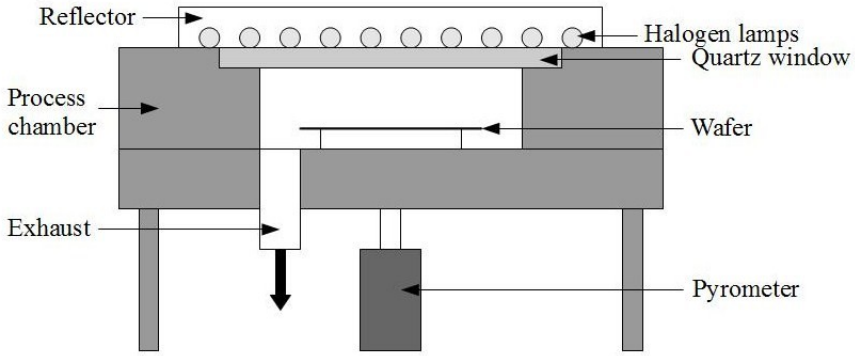

Figure 3.4: Schematic of the JetFirst 100 RTP

The RTP used in this work houses a single wafer cold wall reaction chamber. An array of twelve tubular halogen lamps in the furnace is used to heat a sample in the process chamber. The two regions are separated by a quartz window. The lamps emit

infrared radiation which is measured by a pyrometer, calibrated (HT100 calibration) to give an accurate measure of the temperature in the chamber. The chamber is water cooled and the gas is injected underneath the wafer, circulating around it.

The anneals started with one minute at 20^{o}C and a N_2 flow at 1000 sccm to purge the chamber before the heating began. The temperature was then ramped up to the target temperature, held there for the allotted time and brought down again, all with a N_2 flow at 500 sccm. There was an intermediate step from 350^{o}C to 500^{o}C for 30 seconds to alleviate the risk of power spikes when the pyrometer switched on. The ramp rates were typically between 10 and 20^{o}C/s

Chapter 4: Characterization Techniques

Once the silicon-rich silicon nitride films were prepared, they needed to be analyzed. First the composition of the films after implantation was determined by Rutherford backscattering spectrometry (RBS). Next, since the goal of this work is to make an efficient light emitter, we clearly needed to obtain the spectrum of light emitted from the samples. This was measured with photoluminescence spectroscopy (PL). Transmission electron microscopy (TEM) was utilized to attempt to directly view any silicon nanoclusters in the SRSN films. Lastly, the electronic structure and bonding arrangement of the Ce-doped films were determined by using x-ray absorption spectroscopy (XAS).

4.1 Rutherford Backscattering Spectrometry

Rutherford backscattering spectrometry (RBS) is a method of measuring the composition of a sample as a function of depth. It was used in this work to confirm the existence of excess silicon in the films after ion implantation.

The technique relies on a very high energy beam (typically ~1-3 MeV) of light ions such as $^4He^+$. These ions are able to penetrate thousands of Angstroms deep into a target film and cause negligible sputtering of the surface atoms. The incoming ions lose energy in the material through electronic excitation and ionization of the target atoms. This energy loss can be considered continuous with depth into the target material. The

ions can also be scattered off the nuclei of the much heavier target atoms (Rutherford scattering). If the incoming ion has mass M_o and initial energy E_o, its energy after scattering off of a surface atom of mass M is

$$E = \left(\frac{(M^2 - M_o^2 sin^2\theta)^{1/2} + M_o \cos\theta}{M_o + M} \right)^2 E_o \tag{4.1}$$

which decreases with increasing M [64]. Therefore the energy of backscattered ions will decrease with decreasing mass of the target atom and with increasing depth. The energy of the backscattered ions can then be measured with a detector to obtain a spectrum yielding information on the composition as a function of depth.

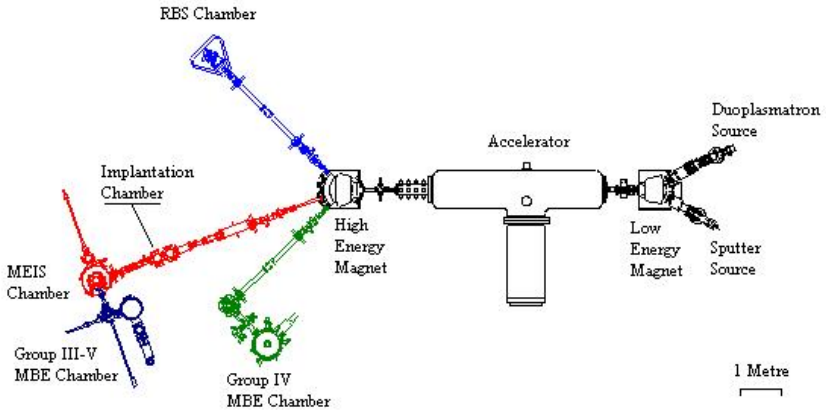

Figure 4.1: UWO's Tandetron Accelerator Laboratory [71]

Measurements were made with the 1.7 MV Tandetron Accelerator at the University of Western Ontario. A schematic of the accelerator and beam lines is shown in Fig. 4.1. For all the samples the ions were detected until the total dose collected was 4.0 μC. This resulted in an acquisition time of typically around 1440 s.

The collected spectrum was analyzed using SIMNRA software. The composition of the sample was determined by fitting a simulated spectrum to the experimental one.

4.2 Photoluminescence Spectroscopy

In general it is much easier to excite the electrons in a material optically rather than electrically. This is due to the fact that photons enter a material and transfer their energy to electrons directly, whereas suitable carrier injection, which is essential to exciting electrons electrically, is not always attainable due to the band structure of the material. In this work, a study of the electrical characteristics of the films was not undertaken. Instead, photoluminescence spectroscopy (PL) was used to characterize the optical properties of the films.

The steps that occur in PL are as follows. First, an incident photon whose energy is greater than the band gap of the material is absorbed by a valence electron, which is then excited to the conduction band creating an electron-hole pair (EHP). Next, the electron then gives up energy to the lattice until it is near the bottom of the conduction band. In section 2.2 it was stated that the EHP can then recombine two different ways: (1) directly across the band gap so that a photon with energy equal to the band gap energy is given off, or (2) by way of a mid-gap defect state so that a photon with energy less than the band gap energy is given off [72]. In a PL setup a detector is then used to collect the emitted light.

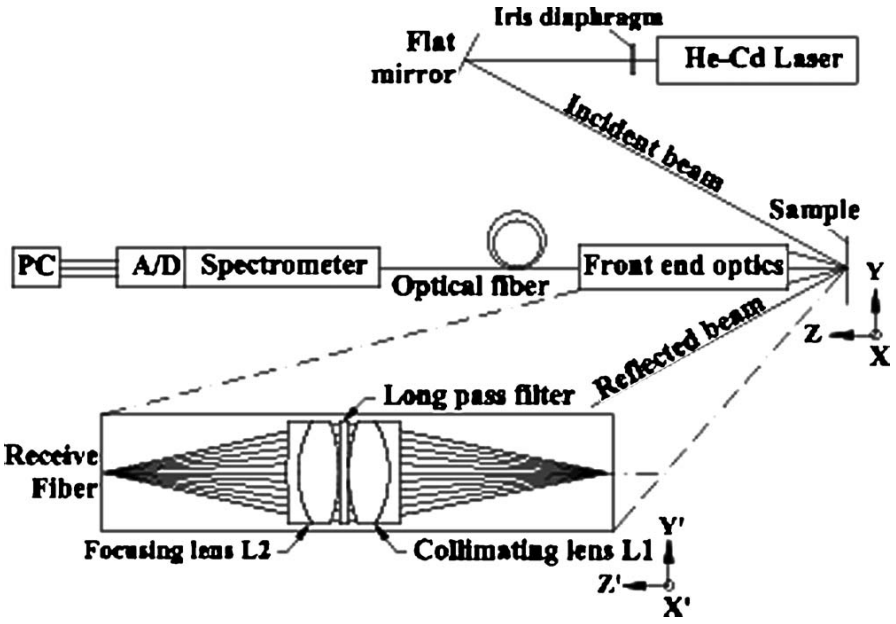

Figure 4.2: Schematic of the PL setup used in this work [73]

A schematic diagram of the PL setup used is shown in Fig 4.2. The details of this PL system are outlined in [73]. A 325 nm He-Cd laser is used as the pump source, while an Ocean Optics S2000 spectrometer is used to measure the spectrum of emitted light.

Before the measurement, the dark signal must first be accounted for. The dark signal is taken with the lights off and the laser beam blocked. The emission signal must then be tuned to its maximum by using a bright reference sample under continuous scan. Only the X and Y directions of the XYZ stage holder are varied until the emission peak is a maximum. The sample is then measured using a single scan with Scans to Average equal to 5, Smoothing Size equal to 2, and the Nominal Integration Period equal to 2500 ms. To correct for the spectral response of the detector, the original data is multiplied by a correction file, effectively converting the output power to photon flux.

4.3 Transmission Electron Microscopy

To provide more direct evidence of the presence of silicon nanoclusters, the films were analyzed using transmission electron microscopy (TEM). Two different microscopes were used: a 120 keV Phillips CM12 for low resolution images and a 300 keV FEI Titan 80-300 for high resolution electron microscopy (HREM) imaging. Both of these microscopes are located in the Canadian Centre for Electron Microscopy (CCEM) at McMaster University.

Electron microscopes are capable of much higher resolution than optical microscopes because of the small wavelength of electrons when accelerated through a high voltage. From the equation for the de Broglie wavelength of an electron (2.5) we can see that at higher energies (and higher momenta) the wavelength decreases. Taking into account relativistic effects, the wavelength of an electron with kinetic energy equal to E is

$$\lambda = \frac{h}{\sqrt{2m_e E\left(1 + \frac{E}{2m_e c^2}\right)}} \tag{4.2}$$

where h is Planck's constant, m_e is the rest mass of an electron and c is the speed of light [74]. For example, at 120 and 300 keV (the maximum energies of the microscopes used) the electron wavelength is 3.3 and 2.0×10^{-3} nm respectively, much smaller than the wavelength of visible light.

To see why using a beam of electrons in a microscope results in a higher resolution than visible light, we can refer to the Rayleigh criterion for visible light microscopy:

$$\delta = \frac{0.61\lambda}{\mu \sin \beta} \tag{4.3}$$

This states that with the wavelength of the light λ, the refractive index of the medium μ and the semi-angle of collection of the magnifying lens β, δ is the smallest distance that can be resolved. Similarly, for TEMs δ can be approximated as

$$\delta \cong \frac{1.22\lambda}{\beta} \tag{4.4}$$

As an example, using green light with a wavelength of about 550 nm, the smallest distance that can be resolved is about 300 nm. This is much too large to image nanoclusters, which are typically on the order of a few nanometres. However, using an electron beam with a wavelength of about 2.0×10^{-3} nm, theoretically the smallest distance that can be resolved is less than one Angstrom. In practice this limit cannot actually be reached as it is not possible to build perfect electron lenses, though TEM can be used to image objects on the order of a few nanometres, such as silicon nanoclusters.

A TEM can be operated in two different modes: diffraction pattern formation mode and image formation mode. The ray diagrams for these two modes are shown in Fig. 4.3. In the diffraction mode the back focal plane (BFP) of the objective lens acts as the object plane of the intermediate lens and a diffraction pattern is projected onto the viewing screen. In the image mode the image plane is the object plane of the intermediate lens and an image is projected onto the viewing screen.

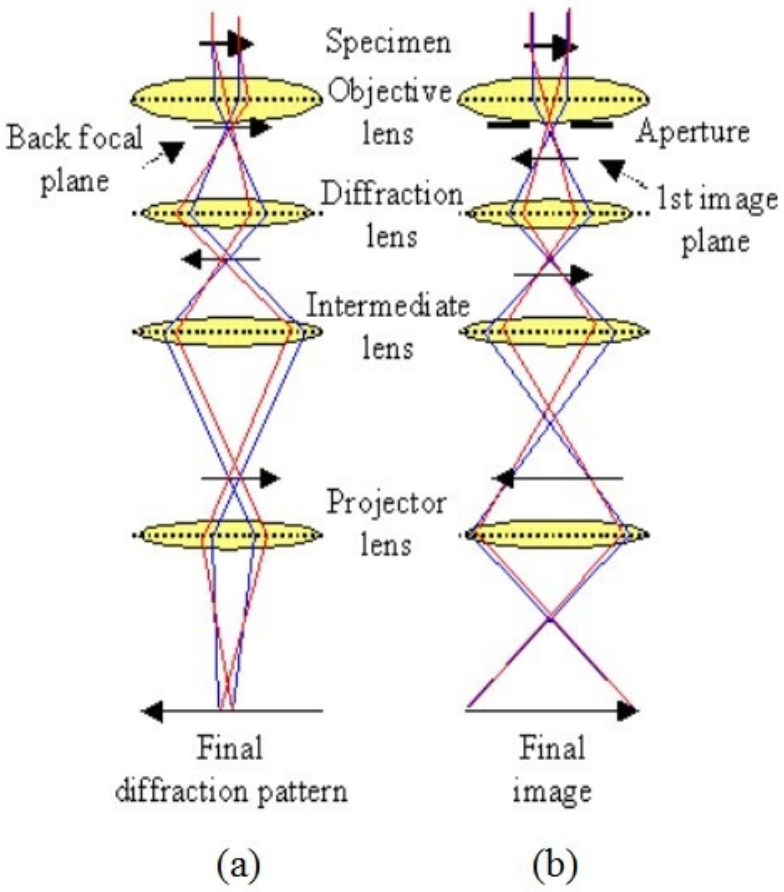

Figure 4.3: The two different modes of TEM. (a) diffraction mode; (b) image mode [75]

In conventional TEM, the two methods of image formation are bright-field (BFTEM) and dark-field (DFTEM). In both cases an objective aperture is placed in the BFP of the objective lens. The difference is that in BFTEM (the method used in this work) only the undiffracted electron beam passes through the aperture and crystalline regions appear dark, while in DFTEM the aperture is used to select one of the diffracted beams and only the regions that diffract appear bright.

In addition to conventional TEM imaging, high-resolution imaging (HRTEM) was performed on the FEI Titan 80-300 microscope. The high resolution images are obtained by using two beams (the transmitted and the diffracted beams) which interfere with each other. By knowing that the diffraction pattern is related to the Fourier transform of the real space atomic arrangement, the interference pattern can be used to find the real space structure. By sampling a larger section of the reciprocal space, higher resolution can be achieved. In fact, resolution below one Angstrom is now possible.

The samples that had previously been annealed and analyzed with RBS and PL had to be specially prepared for the TEM. This was to ensure the film was thin enough to be transparent to electrons so that details inside the film were discernible under the microscope. The full details of the procedure are given in several guides available at the CCEM.

Two, 1 mm wide, 1 cm long samples were cut from the original cleaved sample using a diamond saw. The two pieces were glued together with the films facing each other, and three more 1 mm x 1 cm silicon pieces were glued on either side for support. The glue was made by mixing the resin and hardener in a 10:1 ratio. The sample was then grinded down on both sides using different grit sandpapers until the thickness was about 100-150 μm. Two circular samples were cut from this using an ultrasonic cutting device and a metal moly ring was glued on each one for support. The sample with moly ring was then polished down further with a Fischione Dimpler to about 10-15 μm. Finally, the sample was placed in an ion miller until a hole was created in between the two films. The ion miller was set at 4 kV, $\pm 7^{o}$ and 3 rpm. Occasionally additional ion milling was

required. After the ion milling stage a portion of the film was sufficiently thin to be viewed under the TEM.

4.4 X-ray Absorption Spectroscopy

X-ray absorption spectroscopy (XAS) is a characterization technique used to determine information about the local bonding environment in a structure. The information is obtained by observing the details of the absorption edge, the discontinuity where absorption abruptly begins as the energy of the incoming excitation source increases. An example of an absorption edge is shown in Fig. 4.4. The absorption spectrum is typically split into two groups: the region up to ~40 eV above the absorption threshold is the x-ray absorption near edge structure (XANES), and the region beyond that is the extended x-ray absorption fine structure (EXAFS) [76]. For this work, only XANES was used.

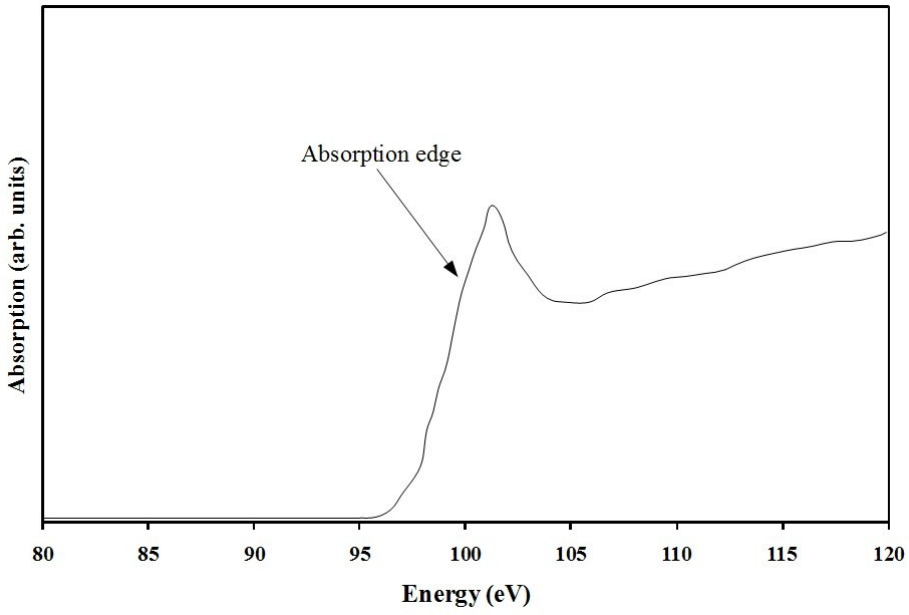

Figure 4.4: A typical XAS spectrum, including an absorption edge (*L*-edge), for silicon

As the name suggests, the method of XAS relies on the absorption of x-rays by the atoms in a structure. An incoming photon, whose energy is equal to or greater than the binding energy of a core electron, excites an electron to the conduction band. That electron will then decay by one of two methods: by directly recombining with a hole and emitting a photon (Fig. 4.5a), or by the Auger process and emitting an electron (Fig. 4.5b). The absorption of the x-rays in the material can be determined by measuring either the emitted Auger electrons, called the total electron yield (TEY), or the emitted photons, called the total fluorescence yield (FLY). The energy of the x-ray beam is scanned over a range to produce an XAS spectrum, with either the TEY or the FLY plotted against the x-ray beam energy.

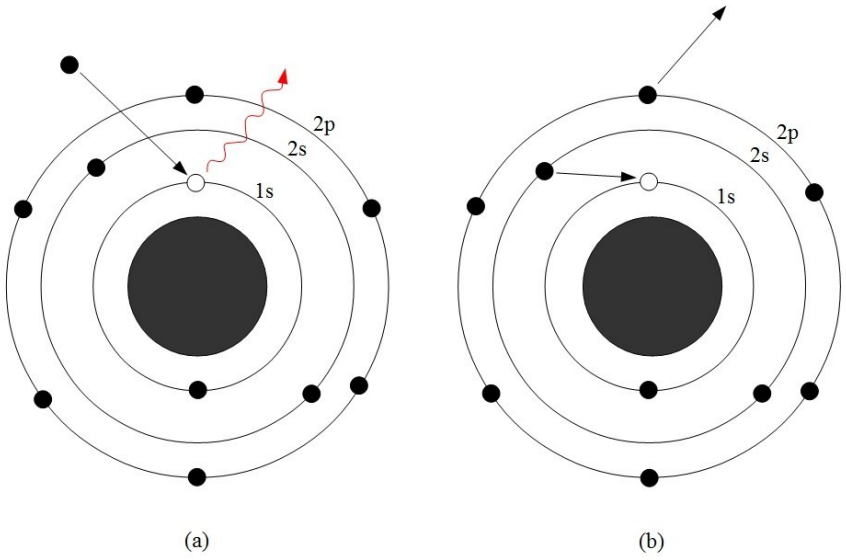

Figure 4.5: The processes of decay in XAS. (a) direct recombination and x-ray emission; (b) Auger recombination

Since electrons are excited to states in the conduction band in XAS, the absorption spectrum will be related to the density of states in the conduction band. However, as the quantum mechanical electric dipole selection rule applies, there must be a change in the azimuthal quantum number:

$$\Delta\ell = \pm 1 \tag{4.5}$$

Therefore, it is actually only the partial density of states that is surveyed. The partial density of states is sensitive to the local electronic structure, so features in the XANES spectrum are sensitive to such things as the coordination of an atom or hybridization. Thus, the XANES spectrum reveals information about the local bonding environment of a structure.

Lastly, an explanation of the XAS nomenclature is necessary before discussing the experimental parameters. The atomic shells going from the innermost outward are named the *K*, *L*, *M* etc. shells. Likewise the absorption edges are named after the atomic shell from which the electrons are excited. For instance, if 1s (*K* shell) electrons are excited, this is the *K*-edge. If 2s or 2p (*L* shell) electrons are excited, this is the *L*-edge.

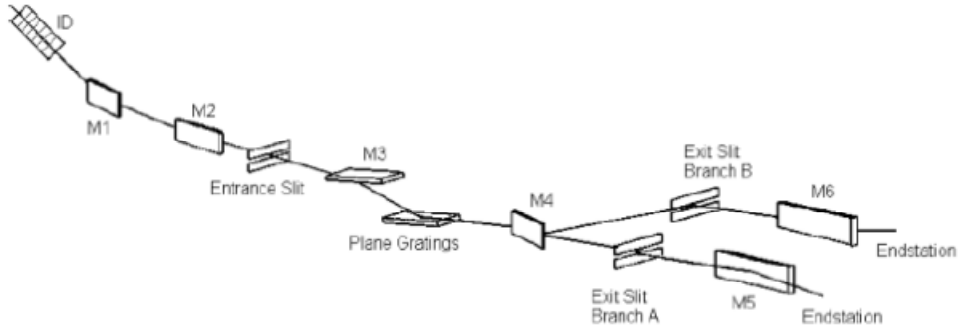

Figure 4.6: Schematic of the VLS-PGM beamline at the CLS [77]

The XAS experiments in this work utilized the synchrotron at the Canadian Light Source (CLS) in Saskatoon, Saskatchewan. The only beamline used was the 11ID-2 variable line spacing plane grating monochromator (VLS-PGM); a schematic is shown in Fig. 4.6. The beamline operates in the energy range of 5.5-250 eV. Only the silicon *L*-edge (2p excitation) was probed, which yields information solely pertaining to silicon bonds. The FLY spectra were used for the analysis.

Chapter 5: Results and Discussion

This research dealt with two types of materials: silicon rich silicon nitrides and cerium doped silicon nitrides. The bulk of this work deals with SRSN grown by ICP-CVD. Samples from these films were grouped into two categories depending on how the nitrogen was introduced during deposition: plasma and dispersion ring samples. The presence of excess silicon in these films was confirmed by the use of RBS, while the emission spectra were determined from PL measurements. Lastly, TEM imaging was employed in the hopes of finding visual evidence of the formation of silicon nanoclusters in these films.

Cerium doped silicon nitrides were also investigated. PL measurements were used to determine the emission spectra of samples with Ce implanted into both stoichiometric silicon nitride and SRSN. X-ray spectroscopy was used to study the bonding environment of the films.

One final aspect of this work was to investigate how these films compared to ones deposited by LPCVD, both SRSN and Ce-doped silicon nitride films. Only PL was used in this context.

5.1 Silicon Rich Silicon Nitrides

The following section presents the results from the analysis of the SRSN films. This involved the composition and luminescence properties of the films, as well as imaging them with TEM.

5.1.1 RBS Results

Rather than making the SRSN films purely by deposition, the films were made by first depositing a stoichiometric Si_3N_4 film by ICP-CVD or LPCVD and then implanting the excess silicon which was utilized in forming the silicon nanoclusters. One would want to confirm that this was indeed what occurred, that there is in fact excess silicon in the films. RBS was used to verify this as it determines the composition of the film as a function of depth, so ideally the implantation profile of the implanted silicon should be observable.

It is important to remember that the ICP-CVD films had been formed in two different ways, by introducing the nitrogen either through the plasma or through the dispersion ring. So in addition to observing the excess silicon, there is another need for using RBS. Comparing the compositions of these films could yield insight into the difference in the formation of these films and in particular, how nitrogen incorporates during growth.

The raw RBS data from plasma and dispersion ring samples is shown in Fig. 5.1. Both samples were implanted with silicon at a fluence of 4.2×10^{16} cm^{-2}. Neither of the samples had been annealed after implantation. SIMNRA was used to model the composition of these films; the simulated data is also shown in Fig. 5.1. Since the

estimates from the SRIM software suggested most of the implanted ions would stop in the upper half of the film, the samples were modeled using three layers. The modeled film was split into two layers, the top one being more silicon rich than the bottom one. The third and final layer was the silicon substrate. This model provided a reasonable fit to the raw data with the appropriate choice of constituent concentrations. These concentrations are given in Tables 5.1 and 5.2.

Element	Concentration		
	Layer 1 (top of film)	**Layer 2 (bottom of film)**	**Layer 3 (substrate)**
Si	0.43	0.37	1.00
N	0.27	0.33	0.00
O	0.16	0.16	0.00
H	0.14	0.14	0.00

Table 3.1: Concentrations of elements in the dispersion ring films, as used in SIMNRA

Element	Concentration		
	Layer 1 (top of film)	**Layer 2 (bottom of film)**	**Layer 3 (substrate)**
Si	0.41	0.33	0.95
N	0.33	0.41	0.00
O	0.12	0.12	0.00
H	0.14	0.14	0.05

Table 5.2: Concentrations of elements in the plasma films, as used in SIMNRA

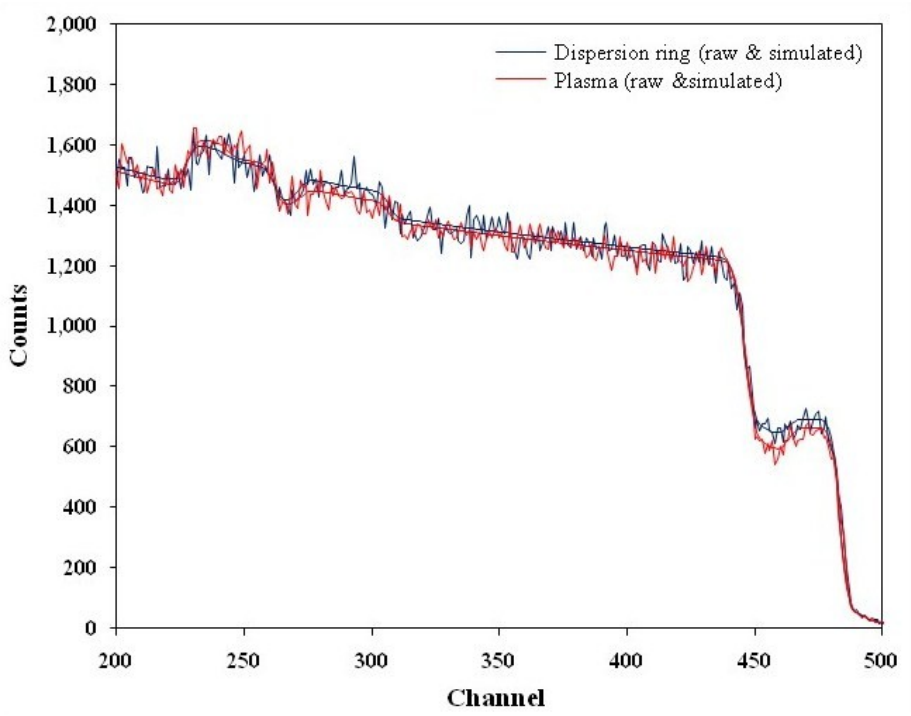

Figure 5.1: Raw and simulated RBS spectra

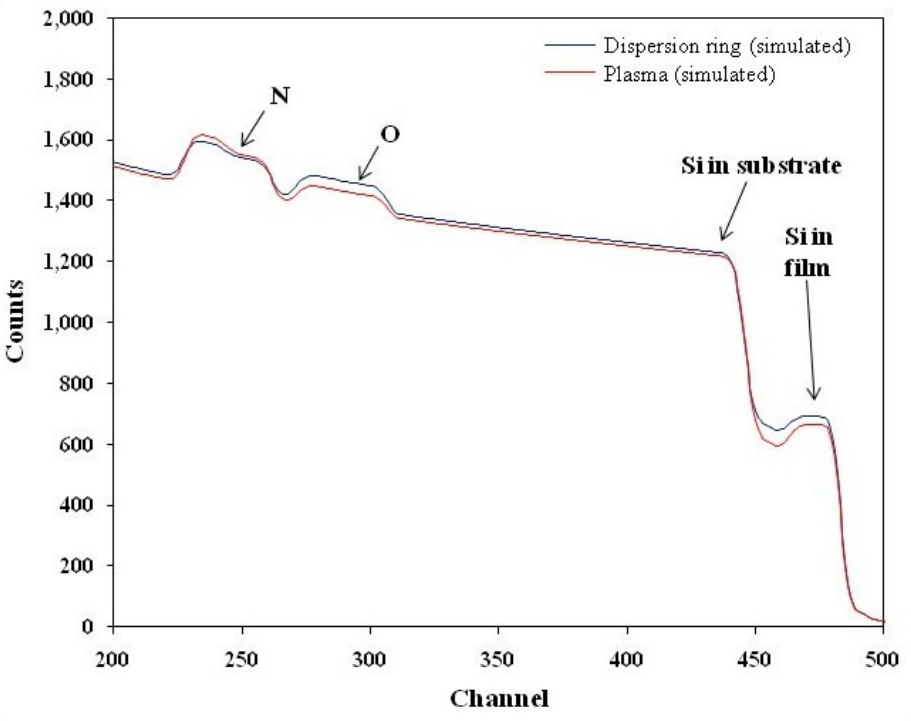

Figure 5.2: Simulated RBS spectra with peaks labelled

The simulated data is shown again alone in Fig. 5.2 and the peaks are labelled for more clarity. Going from right to left, the first peak is from the silicon in the film, the second peak is from the silicon in the substrate, the third peak is from the oxygen in the film, and the last peak is from the nitrogen in the film. Oxygen was not intentionally added to the film but oxygen contamination is common in the ICP-CVD system used.

The most important feature is the dip in the "silicon in film" peak. The silicon concentration is higher closer to the surface; deeper into the film, the composition is closer to being stoichiometric. This shows that there was in fact excess silicon implanted into the film as we can see a region of higher silicon concentration. This is important because we now know that we have excess silicon available to form nanoclusters, and so with annealing nanocluster formation should occur.

There is also a slight difference between the plasma and dispersion ring samples. The depth to which the "silicon in film" peak extends differs, suggesting a difference in silicon concentration between the two films. We can calculate the excess silicon concentration as a percentage by using the formula

$$Si_{ex} = \frac{Si_{at.\%}}{(Si_{at.\%} + N_{at.\%})} - \frac{3}{7} \tag{5.1}$$

from Wilson's study of the effects of thermal treatments on SRSN films [78]. Using this equation, the excess silicon in the dispersion ring sample is approximately 14% and in the plasma sample is approximately 7%. These values are estimates due to the errors involved in simulating the RBS spectra, though they still do show the difference in excess silicon concentration between the two samples.

The excess silicon concentration was calculated using the "silicon in film" peak discussed earlier; however, in the context of nitrogen incorporation into the film, it is more natural to observe the nitrogen peak. In this case, in the lower part of the film (which has less implanted silicon and therefore the nitrogen concentration should be closer to that of the deposited film) the nitrogen concentration is higher for the plasma sample. Therefore, though both types of films were intended to be stoichiometric, at least one was not. Either the dispersion ring samples are silicon rich or the plasma samples are nitrogen rich.

The difference in silicon and nitrogen concentrations can be better understood when we revisit the refractive indices given in section 3.1.1. The refractive index of the dispersion ring samples was 1.92 whereas the refractive index of the plasma samples was 1.75. The refractive indices of Si_3N_4 and SiO_2 are 2.05 and 1.46 respectively [1], and the refractive index of pure silicon is 3.88. Judging by these values, it appears as though the dispersion ring samples have a higher silicon concentration as their refractive index (1.92) is closer to that of pure silicon (3.88), agreeing with the analysis of the RBS data. It does appear that both the dispersion ring and plasma samples are actually nitrogen rich, given the fact that both of their refractive indices are lower than that of Si_3N_4 (2.05), but one must remember the oxygen that was detected in the RBS measurements (Fig. 5.2). Since the refractive index of SiO_2 is only 1.46, the presence of oxygen in these films would lower their refractive index. However, the density of the films, which can greatly depend on the deposition parameters, will also affect its refractive index, so one must be careful not to read too much into the difference between the refractive indices.

From the RBS and ellipsometry data, it is believed that with the gas flow rates given in section 3.1.1 on the ICP-CVD system, introducing the nitrogen through the dispersion ring will yield a stoichiometric silicon nitride (Si_3N_4) film. If the nitrogen is introduced through the plasma, the ionized species more readily incorporate into the film and therefore the film is nitrogen rich. In addition, implanting silicon ions into the film will add excess silicon which theoretically should be available for nanocluster formation. Whether the nanoclusters do in fact form and emit light was determined from PL and TEM.

5.1.2 PL Results

So far only the composition of the films has been analyzed, yet if one wants to utilize a material as a light emitter, naturally the emission spectra of said material should be investigated. Photoluminescence spectroscopy was used as it is much easier to excite a material by photoluminescence than by electroluminescence (EL). In fact, just because a material exhibits strong PL characteristics, does not mean this will translate to EL, which is the process exploited in light emitting devices. Therefore, this work mainly shows what kind of emission is possible if at all, and uses the spectra to draw a conclusion about possible nanocluster formation.

In the following section the PL results from the SRSN films grown by ICP-CVD are given. These include PL spectra after isothermal anneals varying the implantation fluence or annealing time, isochronal anneals varying the anneal temperature, and annealing in forming gas. In section 5.1.2.2 the PL results from the SRSN films grown by

LPCVD are given. These samples all had the same implantation fluence and annealing time, but varied the anneal temperature.

All the PL spectra are plotted on a linear scale. The scales for the dispersion ring and plasma samples' spectra are roughly the same.

5.1.2.1 ICP-CVD films

In investigating the PL characteristics of the silicon nitride films, there were a few different degrees of freedom in the fabrication process that needed to be sampled in addition to the previously discussed methods of nitrogen incorporation. The fabrication of the samples always started by depositing a stoichiometric silicon nitride film with ICP-CVD (with the N_2 through either the plasma or the dispersion ring), but then changes could be made in the fluence of implanted silicon ions and the annealing time and temperature. Naturally these parameters were varied until peak luminescence occurred.

The first parameter varied was the implantation fluence. Eight films were made (3 dispersion ring, 5 plasma) at fluences of 0.8, 1.6, 3.2, 3.8, 4.2, 4.6, 5.0 and 10×10^{16} cm^{-2}. These were all annealed for 1 minute in N_2 at temperatures ranging from 600°C to 1100°C. The PL spectra for all these samples are not given here, instead they are given for one temperature. Fig. 5.3 shows the PL intensity for dispersion ring films implanted with different amounts of excess silicon and all annealed at 600°C for one minute. All the samples displayed a red shift at higher anneal temperatures and higher fluences, and the anneal temperature at which peak luminescence occurred decreased with increasing fluence. The change in intensity and emission energy is evident even in Fig. 5.3 which just shows the samples annealed at 600°C.

The peak luminescence for each film, between 350 nm and 750 nm, is given in Fig. 5.4. It is important to note that these points are at different anneal temperatures for the two different types of films because the maximum PL intensity occurred at different annealing temperatures. As well, this is not an integration of the PL spectra but rather simply the peak point. It is not useful in quantitative calculations but more to qualitatively determine the general range of implantation fluences in which the most luminescence can be obtained.

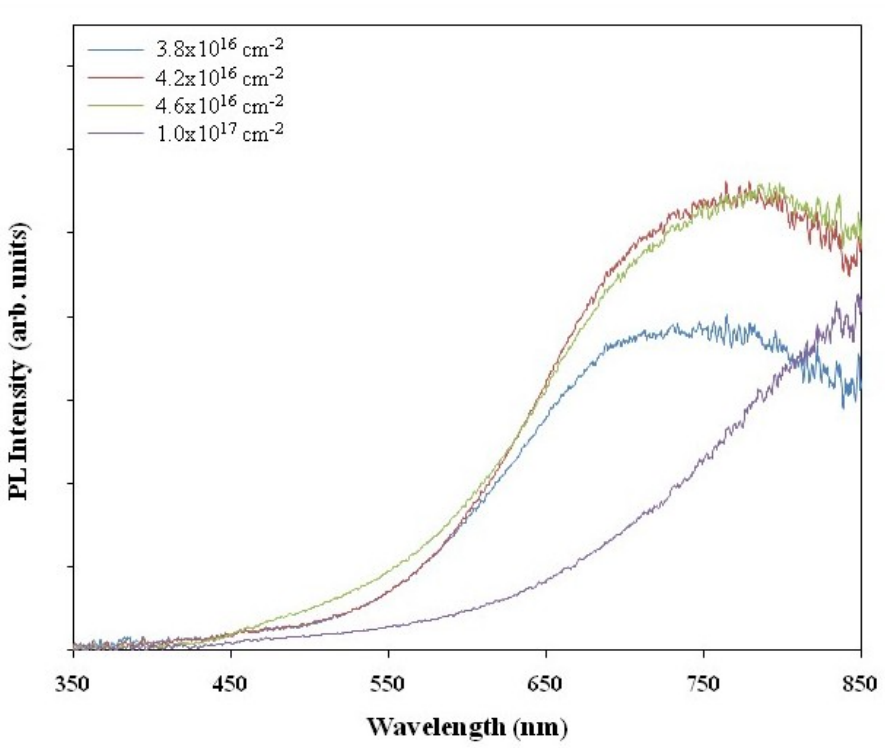

Figure 5.3: PL spectra of dispersion ring samples annealed at 600°C

In Fig. 5.4 one can see that the PL intensity increases up to a maximum point and then decreases again at higher fluences. This can be explained qualitatively by the growth of silicon nanoclusters within the silicon nitride film. With very little excess silicon in the

film there are few nanoclusters and so the PL intensity is still relatively low. As the excess silicon increases the PL intensity will also increase because more nanoclusters are able to form. As more excess silicon is added these become larger, which is why there is a red shift at higher fluences, exhibited in Fig. 5.3. At some point the nanoclusters will grow large enough that their emission moves into the infrared region, and eventually the

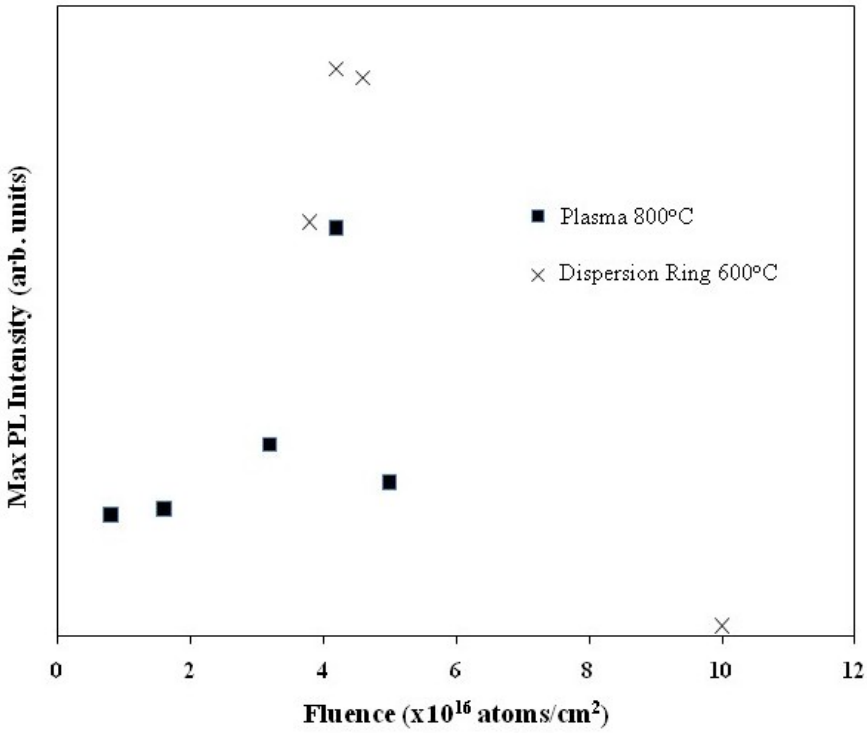

Figure 5.4: Maximum PL intensity (between 350 nm and 750 nm) of samples with varying excess silicon concentrations

nanoclusters will start merging and showing bulk characterics, so the efficiency of the emission will decrease. Thus, in any system with embedded silicon nanoclusters, the luminescence is expected to increase with increasing excess silicon concentration to a maximum, and then decrease again at very high excess silicon concentrations. This is the

behaviour that was observed, and since the PL setup only measures in the visible region, the measured PL intensity decreases from the maximum when the emission moves into the infrared region.

This behaviour of the PL intensity as a function of excess silicon concentration does suggest the presence of nanoclusters formed from the excess silicon. It appears as though the maximum luminescence from these nanoclusters occurs for fluences around $4.0\text{-}4.5\text{x}10^{16}$ cm^{-2}. Consequently, all further studies used samples with implanted silicon fluences around that range to ensure there would be the maximum possible emission.

So far it has been shown how the amount of excess silicon affects nanocluster emission, next is to determine the dependence on annealing. Theoretically, a longer anneal should allow more nanoclusters to grow resulting in an increased PL intensity. As well, the nanoclusters will grow larger, resulting in a red shift in the PL peak. The previous samples had all been annealed for 1 minute, at different temperatures. To observe the dependence of the PL intensity on anneal time, samples from a film with nitrogen incorporated in the plasma were all annealed at $750^{o}C$ for 5 to 60 seconds. The PL spectra from these samples are shown in Fig. 5.5.

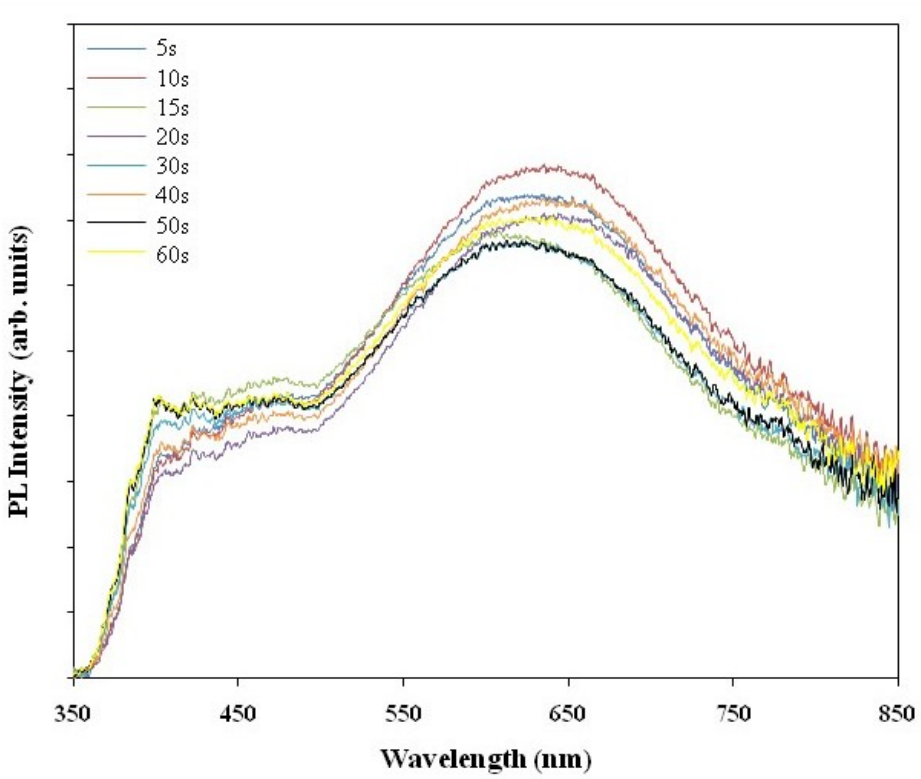

Figure 5.5: PL spectra of plasma samples annealed at 750°C for various times

Contrary to my hypothesis, the PL spectra do not appear to be red-shifted at longer anneals, nor is the emission more intense. This would suggest that all or at least nearly all the nanocluster formation and growth is already complete after 5 seconds. The excess silicon very quickly nucleates into the nanoclusters and there is no more available excess silicon for the nanoclusters to grow after a few seconds. This observation of very rapid nanocluster formation agrees with the findings by Wilson *et al.* [78]. In their study the films were annealed from 2 seconds to 2 hours and though the majority of nanocluster formation occurred in the first two seconds, there was still a slight red-shift at longer anneals. This suggests that after the transient excess silicon diffusion, nanocluster growth

in silicon nitrides is primarily due to Ostwald ripening effects, as has been seen in silicon oxide for progressively higher anneal temperatures [37]. However, for the purposes of this work, a short anneal would suffice. Consequently, with all subsequent annealing studies, the samples were annealed for one minute.

Next, isochronal anneals of 1 minute were performed on dispersion ring and plasma films with silicon implantation fluences of 4.2 and 4.5×10^{16} cm^{-2}. The PL spectra from these samples are shown in Figs. 5.6-5.9. It is worth noting that there is no luminescence in the as-implanted samples. It is not expected that silicon implanted at room temperature would be able to form nanoclusters, as is the case with CVD grown SRSN films where nanocluster emission is observable in as-deposited samples [79]. However, ion implantation damages the crystal structure of the film causing defects, though, in the case of silicon nitrides it appears there are no radiative defects present after implantation. In fact, for there to be luminescence from as-implanted SRSN films, the implantation must be performed at a higher temperature to induce nanocluster formation [44]. This is in contrast with silicon oxides which can display several PL bands in as-implanted samples after room temperature implantation [35]. Therefore, the defects induced by implantation in silicon nitrides are most likely nonradiative recombination centres which disappear with subsequent annealing.

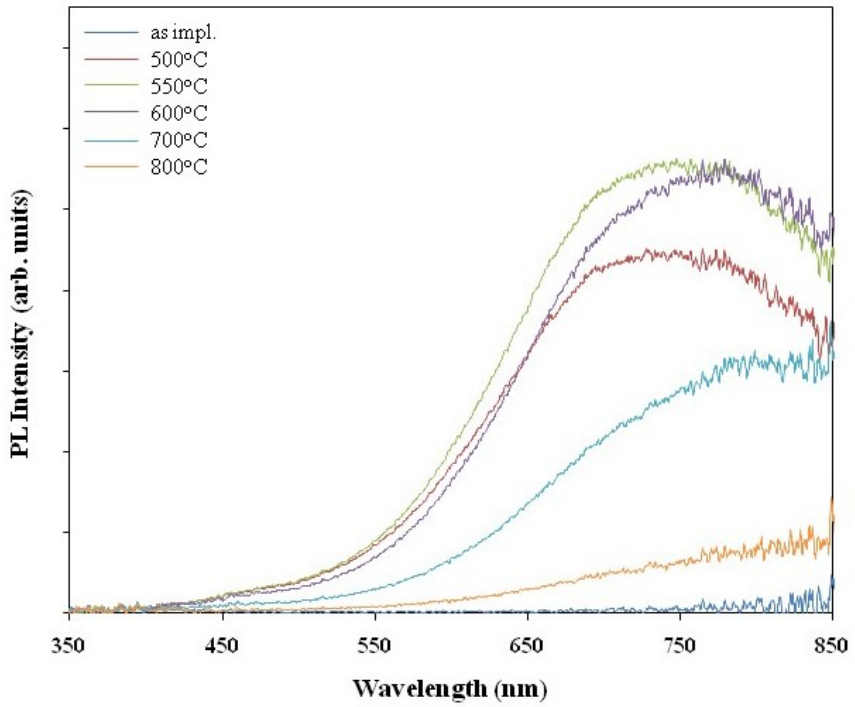

Figure 5.6: PL spectra of dispersion ring samples with silicon fluence of $4.2x10^{16}$ atoms/cm^2

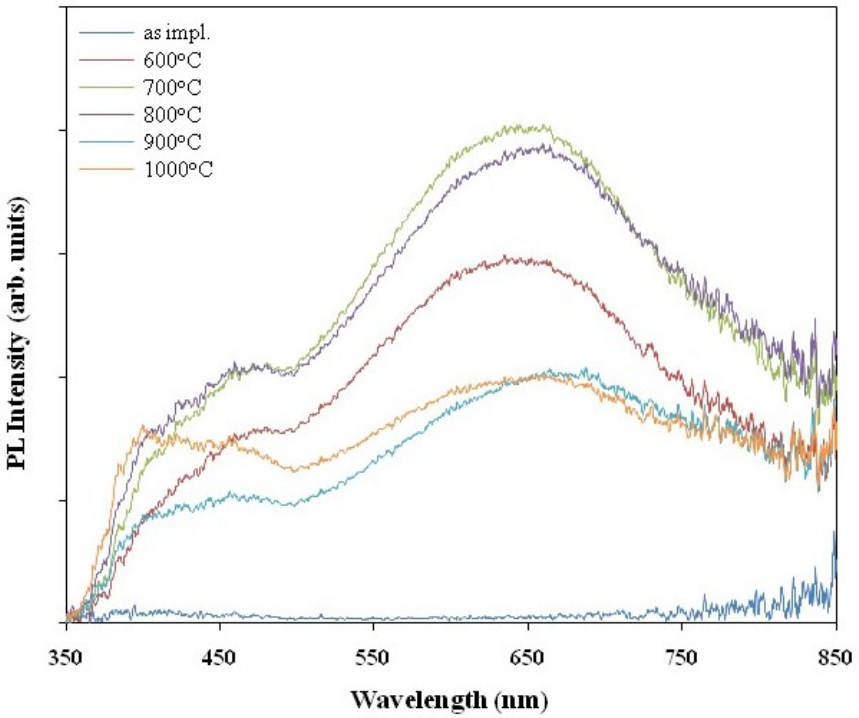

Figure 5.7: PL spectra of plasma samples with silicon fluence of $4.2x10^{16}$ atoms/cm^2

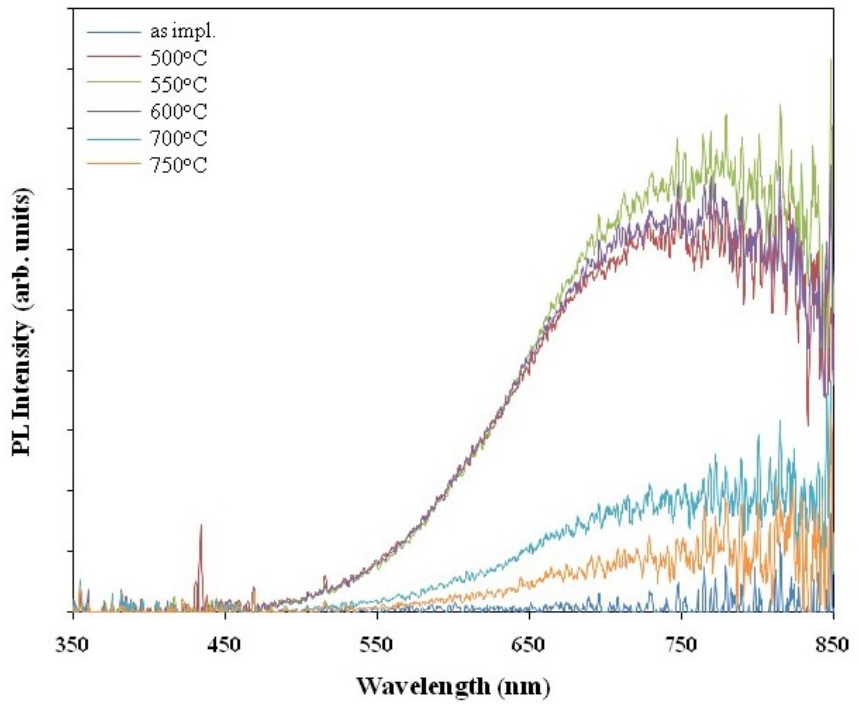

Figure 5.8: PL spectra of dispersion ring samples with silicon fluence of $4.5x10^{16}$ atoms/cm^2

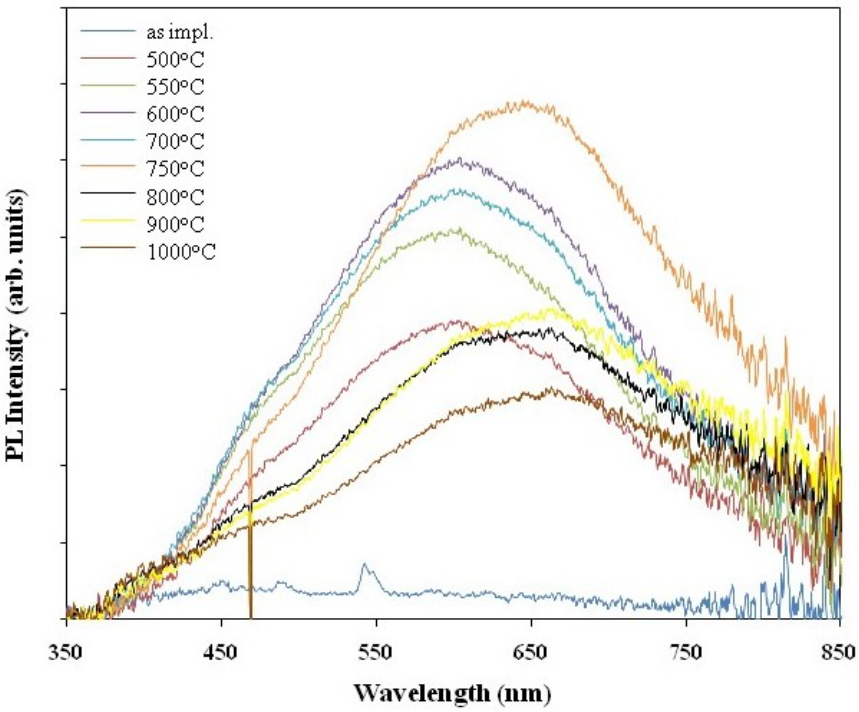

Figure 5.9: PL spectra of plasma samples with silicon fluence of $4.5x10^{16}$ atoms/cm^2

An important feature of these PL spectra is that the main peak is red-shifted at higher anneal temperatures in all cases, particularly for the dispersion ring samples in Fig. 5.6 and the plasma samples in Fig. 5.9. This is evidence that there is nanocluster formation in these films and the clusters are at least the primary, if not only, cause of the luminescence.

Though the spectra all exhibited this red-shift, there are also considerable differences in the spectra of the dispersion ring samples (Figs. 5.6 & 5.8) and the plasma samples (Figs. 5.7 & 5.9). The luminescence from the dispersion ring samples peaks at a longer wavelength than the plasma samples, around 750 nm. According to the Brus model, longer wavelength emission would correspond to larger nanoclusters. The RBS data did show that the dispersion ring samples were more silicon rich, but that could result in more nanoclusters of a similar size. However, it has already been mentioned that Ostwald ripening plays an important role in nanocluster growth, so the formation and growth of silicon nanoclusters in the dispersion ring samples can most likely be summarized as follows. In the first few seconds of the anneal the excess silicon quickly nucleates into many nanoclusters. Because of the high density of nanoclusters, there is more Ostwald ripening than in a less silicon rich film, resulting in larger nanoclusters after a 1 minute anneal. At higher temperatures there is still more Ostwald ripening resulting in larger nanoclusters and a red-shift of the PL emission at higher anneal temperatures. In addition, the luminescence appears to be solely from quantum confinement effects within the silicon nanoclusters and not due to radiative defects in the silicon nitride matrix or at the nanocluster-matrix interface.

The PL emission from the plasma samples appears to consist of three peaks: one centred around 600-650 nm, one just below 500 nm, and one around 400 nm. The peak around 600-650 nm is the main peak, with the other two appearing as one large shoulder on the left hand side. The shoulder is most clearly visible in Figs. 5.5 and 5.7. The main peak is the one which exhibits a red-shift at higher anneal temperatures and is attributed to silicon nanoclusters. The emission is at a shorter wavelength than that of the dispersion ring samples. Referring to the previous paragraph, this is explained by the less silicon rich plasma samples growing smaller nanoclusters due to less Ostwald ripening.

The shoulder emission is attributed to defect states, the silicon dangling bonds (K^0 centre) at 495 nm and nitrogen dangling bonds (N_2^0 and N_4^+) at 415 nm [38]. An interesting observation from Fig. 5.7 is that at high temperature anneals (~900-1000^{o}C) the luminescence at the 415 nm peak increases relative to the 495 nm peak. A possible explanation is that as the nanoclusters are growing by Ostwald ripening, there is less interface area and therefore fewer silicon dangling bonds, though this does not explain why there are evidently more nitrogen dangling bonds at higher anneal temperatures. These dangling bond defects can be greatly reduced and the nanocluster emission enhanced by passivating the film with hydrogen, which attaches to the dangling bonds [48].

To investigate the effects of hydrogen passivation, four samples which had previously been annealed at 800^{o}C for 1 minute in N_2 were annealed in forming gas (95% N_2, 5% H_2) at 550^{o}C for 15 minutes. Fig. 5.10 shows the PL spectra from the samples before (darker) and after (lighter) the forming gas anneal. The hydrogen passivation did

decrease the defect emission, though only significantly for the samples with the lowest excess silicon concentration, and it was negligible for the samples with the highest silicon concentration. Interestingly, the main peak was more significantly enhanced at higher excess silicon concentrations. This has been observed before in silicon oxide films and it was attributed to the reduction of nonradiative defects at the nanocluster-dielectric interface or within the silicon oxide matrix [80]. As to why the increase in PL intensity was only observed at high excess silicon concentrations, it is possible that the higher silicon ion fluence caused more implantation damage and therefore more nonradiative defects.

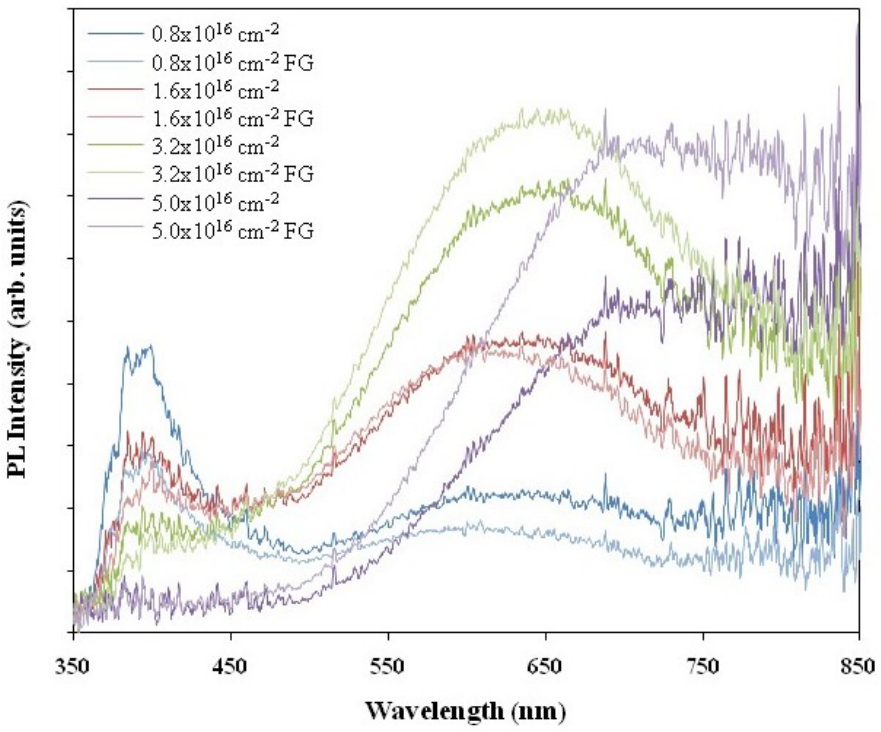

Figure 5.10: PL spectra of plasma samples annealed at 800°C (dark) and after annealing in forming gas (light)

5.1.2.2 LPCVD films

The film deposited by LPCVD was implanted with silicon ions at a fluence of $4.0x10^{16}$ cm^{-2} at 30 keV to be able to compare it with the implanted ICP-CVD films. Samples were then annealed between 500 and 1000^{o}C for one minute. The samples interestingly showed virtually no luminescence at all, despite the fact that similar samples grown by ICP-CVD showed fairly bright luminescence (Figs. 5.6-5.9). This null result was not investigated further, but it is postulated that the ICP-CVD grown films were actually similar to silicon oxynitrides because of the oxygen contamination during deposition. It is possible that the oxygen in those films actually played a crucial role in the luminescence, while in the LPCVD films, which were presumably purely Si_3N_4 (though this was not verified), no luminescence was possible without oxygen present.

5.1.3 TEM imaging

The SRSN films were viewed under two TEMs to try to directly see nanoclusters. It is easier to view nanocrystals as the crystal planes of the nanocrystal are easily recognizable against the amorphous host matrix. However, due to the difference in density between silicon and silicon nitride, amorphous nanoclusters may still be able to be seen. In fact, both crystalline [42] and amorphous [16] silicon nanoclusters have been observed in silicon nitride with TEM.

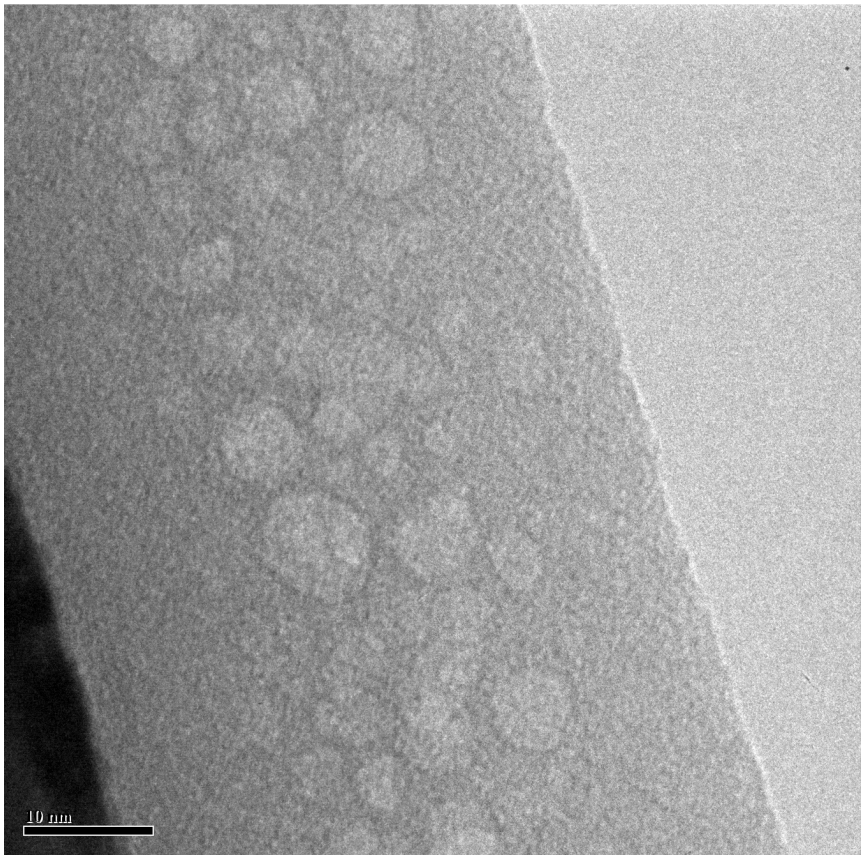

Figure 5.11: TEM image showing possible voids in the film

Using the CM-12 microscope, large artefacts that may be voids due to implantation were easily visible in the plasma sample annealed at 700°C (Fig. 5.11). The spots are on the order of about 5 nm in diameter, most likely a little too large to be nanoclusters, especially since this is the less silicon rich sample. Park *et al.* [16] determined that the energy of emission from amorphous silicon nanoclusters in silicon nitride was related to the nanocluster size by the equation

$$E(\text{eV}) = 1.56 + \frac{2.40}{a^2} \tag{5.2}$$

where a is the diameter of the nanocluster. According to this equation, the nanoclusters in the plasma samples (~550 nm emission) should have a diameter of about 2 nm, while the

nanoclusters in the dispersion ring samples (~750 nm emission) about 5 nm. The density of the spots also seems to be too high for nanoclusters. In addition, these objects are also seen in the dispersion ring sample annealed at 550^{o}C (Fig. 5.12), and their density and size seem to be distributed in a Gaussian distribution along the depth of the film, similar to the implantation profile. Lastly, the spots appear light so they are not very dense, possibly because they consist of a small void. These facts tend to support the argument that the objects are actually voids in the film caused by ion implantation. While the CM-12 showed evidence of implantation damage, it did not have the resolution to show any definite signs of nanoclusters.

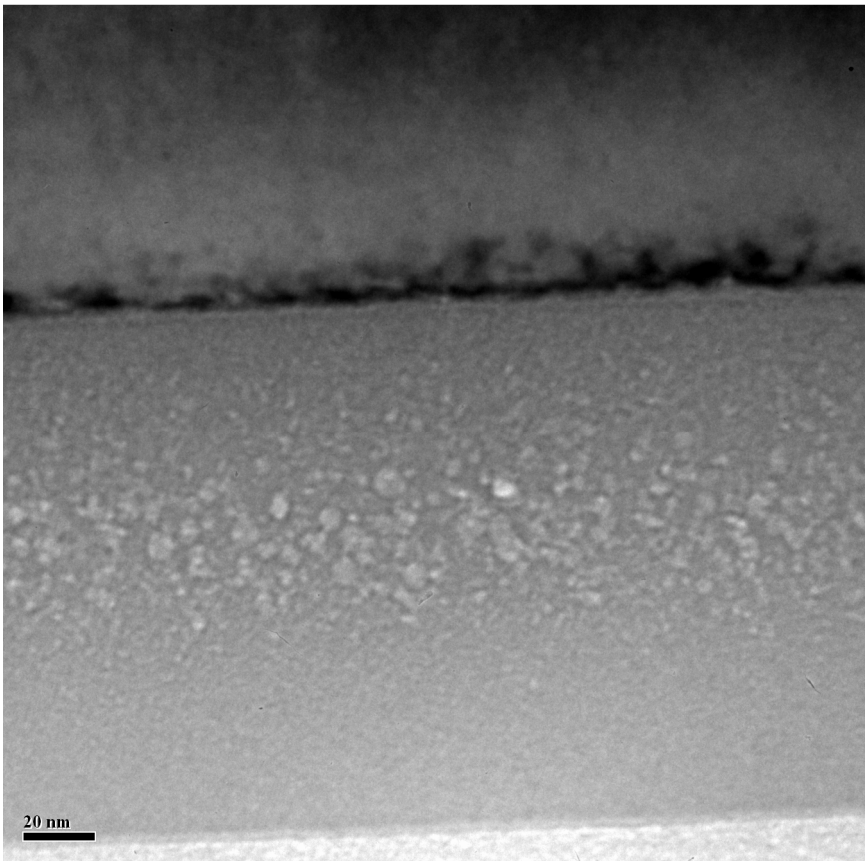

Figure 5.12: Distribution of the artefacts is consistent with the Gaussian profile associated with ion implantation

HRTEM was performed on the FEI Titan 80-300 microscope to obtain definitive proof of nanocluster formation in the SRSN films. These results proved somewhat more promising. Fig. 5.13 shows a dark spot which could be an amorphous silicon nanocluster. However, this spot is still around 5 nm in size and in another plasma (lower silicon concentration) sample, so it is still unlikely to represent a nanocluster. Fig. 5.14 shows another image of the same sample, with the silicon substrate on the right. No spots are clearly visible.

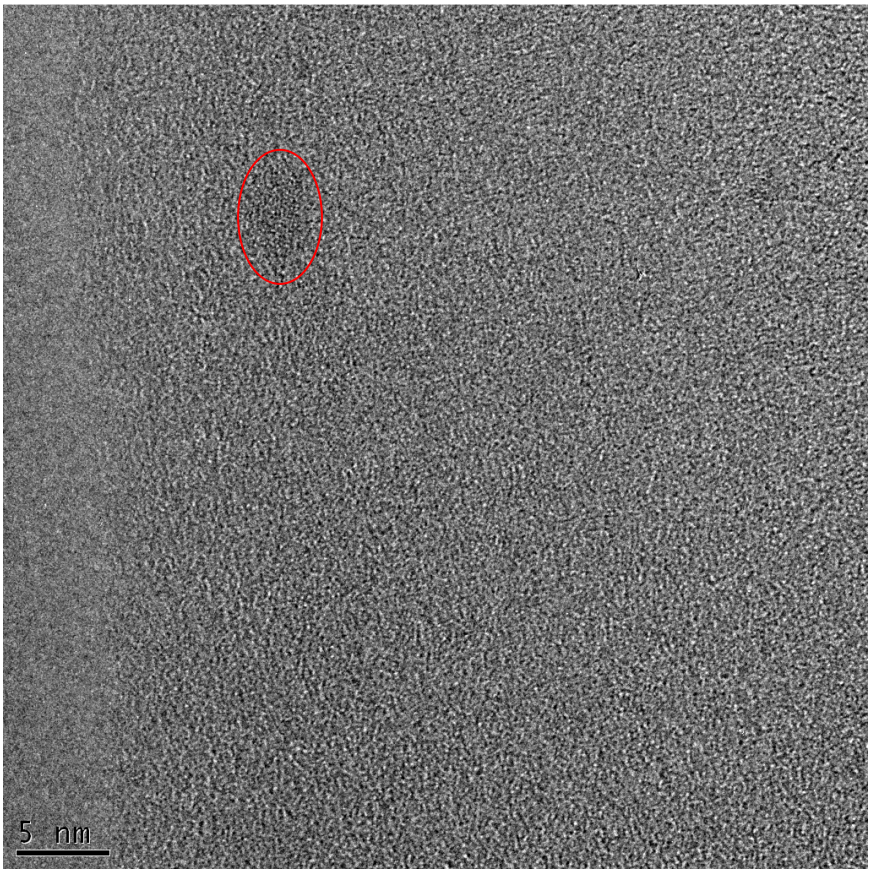

Figure 5.13: Dark spot in top left corner is possibly a nanocluster

The TEM did not show any strong evidence of nanocluster formation, however, as was stated before, amorphous nanoclusters can be very hard to find. At best, we can say there are no nanocrystals in the films, but it is possible that there are amorphous nanoclusters in the films that were just not easily visible.

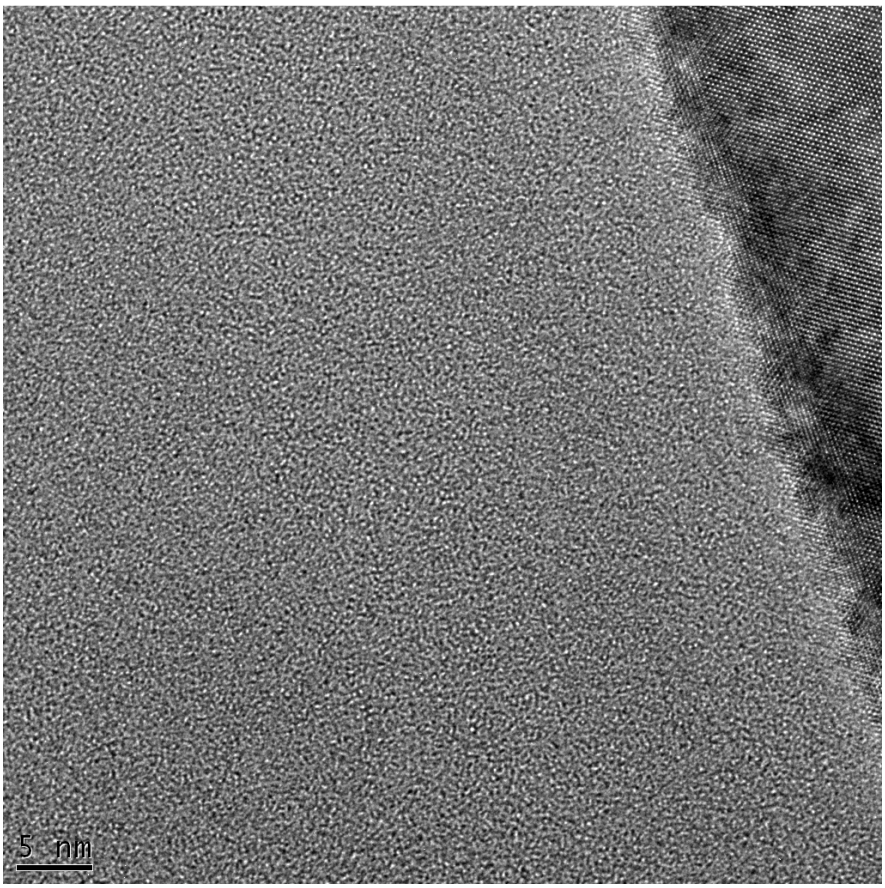

Figure 5.14: HRTEM image of a SRSN film

5.2 Ce-Doped Silicon Nitrides

The following sections present the results from PL and XAS studies of the Ce-doped silicon nitride films. Cerium was implanted at a fluence of 3.0×10^{15} cm^{-2} and an energy of 30 keV into both stoichiometric Si_3N_4 and SRSN. In addition, the same

implantation was done into equivalent films grown by both ICP-CVD and LPCVD, to compare the luminescent properties of differently grown films. The electronic structure of the ICP-CVD grown films was then analyzed using XAS.

5.2.1 PL Results

The next section presents the PL results from Ce-doped silicon nitride films (both stoichiometric and silicon rich) grown by ICP-CVD. Following that the PL results from the LPCVD grown films are presented.

All the PL spectra are plotted on a linear scale. The scales for the spectra of the stoichiometric and silicon rich films are roughly the same, yet are about an order of magnitude greater than that of the SRSN films.

5.2.1.1 ICP-CVD films

The previous studies of SRSN films had already yielded an appropriate silicon implantation fluence which was used for the Ce-doped films. Two stoichiometric silicon nitride films were grown by ICP-CVD, using the dispersion ring to introduce the nitrogen, and one of these was then implanted with silicon at a fluence of 4.5×10^{16} cm^{-2} and an energy of 40 keV. Both of the films were then implanted with cerium and the samples were annealed using the RTP for 5 minutes in N_2 at temperatures of 500°C to 1200°C. The PL spectra from the two sets of samples are shown in Figs. 5.15 and 5.16.

In Fig. 5.15 the PL spectra of the sample with cerium implanted into stoichiometric silicon nitride is shown, and it is clear that the only emission is from the cerium atoms themselves. In Li's work on Ce-doped silicon oxides [55] the PL intensity decreased with annealing between 800°C and 1100°C to a negligible amount, then

increased drastically after annealing at 1200°C due to the formation of a cerium silicate (Fig. 2.18). This behaviour was not observed in our silicon nitride films. It was mentioned earlier that there was some oxygen contamination in these films so it is possible that some cerium silicate was formed after annealing at 1200°C, yet this does not seem to be the primary source of emission. Other than the dip at 800°C, the PL intensity steadily increased with annealing temperature. Li described the decrease in cerium emission until cerium silicate formation as due to the precipitation of cerium ions, so it is possible that cerium ions diffuse less readily in silicon nitride than in silicon oxide. This would mean that the emission is only due to the cerium ions, with the increase in intensity being from the conversion from optically inactive Ce^{4+} to optically active Ce^{3+}, and possibly the formation of some cerium silicate.

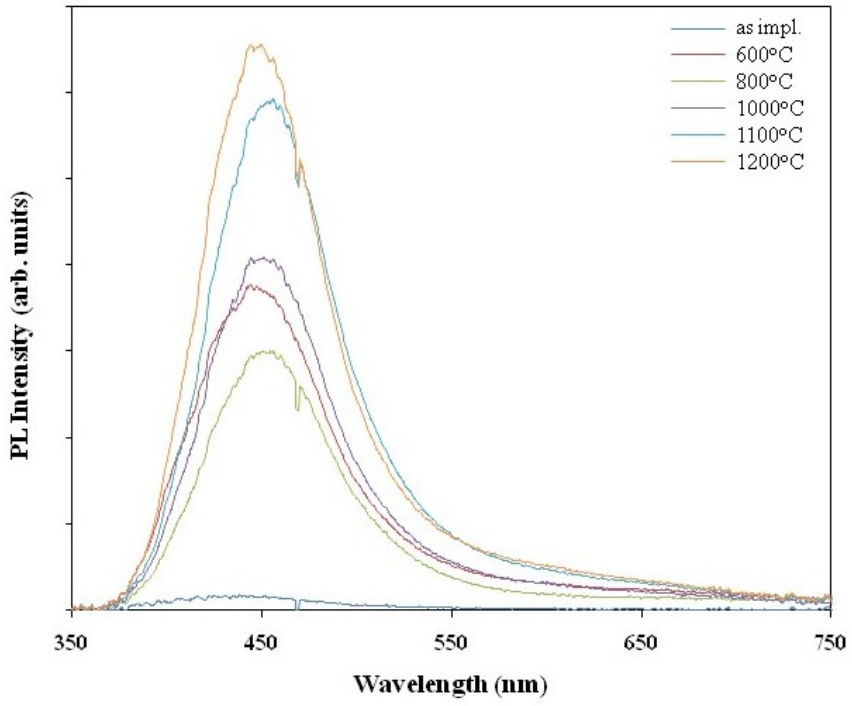

Figure 5.15: PL spectra of Ce-doped stoichiometric silicon nitride samples

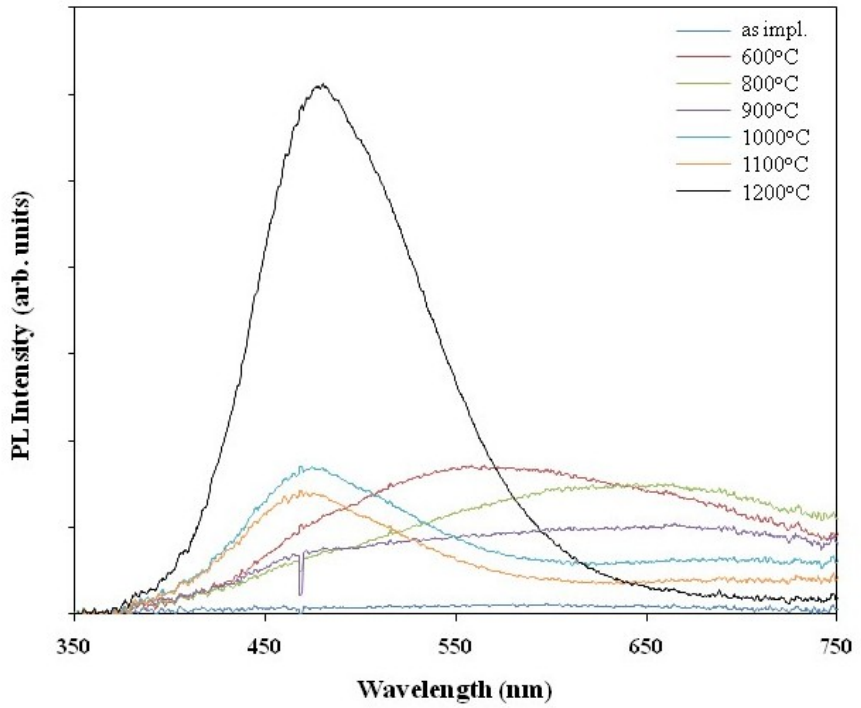

Figure 5.16: PL spectra of Ce-doped SRSN samples

The PL spectra from the sample with cerium implanted into SRSN is shown in Fig. 5.16. After annealing at 600°C a very broad band is visible from about 450 nm to 750 nm. The intensity of this band decreases for annealing at 800 and 900°C, then at 1000°C the band is shifted to a much sharper peak around 470 nm. At 1200°C there is a very large increase in the intensity. The main difference in the PL spectra from these samples and the ones with stoichiometric composition is the apparent existence of silicon nanoclusters in the Ce-doped SRSN samples. The broad band at 600°C is actually comprised of two bands: the cerium emission peak around 470 nm and the nanocluster emission peak around 550 nm, agreeing with the positions of these peaks shown in Figs. 5.15 & 5.9. The

nanocluster peak is red-shifted at higher anneal temperatures, agreeing with previous results.

The Ce^{3+} ions and nanoclusters seem to be two competing sources of emission. Evidence of this comes from the change in the PL spectra after a 1000°C anneal. There is a substantial increase in the cerium emission and decrease in the nanocluster emission. However, from Fig. 5.9 one can see that the nanocluster emission does not decrease to the extent it does in Fig. 5.16 going from 900°C to 1000°C. This behaviour can be explained by assuming the cerium ions are actually embedded inside the silicon nanoclusters after the implantation. At lower anneal temperatures the nanoclusters have a much higher absorption cross-section as the cerium ions are shielded, thus the nanoclusters dominate the emission. At higher anneal temperatures the cerium ions are given sufficient energy to escape the nanoclusters. With the cerium ions no longer shielded, the cerium emission is enhanced at the expense of the nanocluster emission. Therefore, after high temperature anneals, the Ce^{3+} ions in the dielectric dominate the emission. There is also a very dramatic increase in the PL intensity between 1100°C and 1200°C, similar to that observed by Li *et al*. [55]. Because of the oxygen in the films, there could be some cerium silicate being formed, but further analysis would be needed to confirm this.

5.2.1.2 LPCVD films

The films deposited by LPCVD were implanted with cerium ions at a fluence of 3.0×10^{15} cm^{-2} at 25 keV, and one of them was implanted with silicon ions at a fluence of 4.0×10^{16} cm^{-2} at 30 keV. The samples were then annealed between 500°C and 1200°C for five minutes in N_2. Just like the SRSN LPCVD films in section 5.1.2.2, the silicon rich

Ce-doped samples showed virtually no luminescence at all. The film that was only implanted with cerium did show some luminescence after a 1200°C anneal (Fig 5.17). However, it is important to note that this figure is on a much smaller scale than Figs. 5.15 and 5.16. In fact, the maximum PL intensity is about an order of magnitude less than in the previous two figures. As well, since the cerium ions did not emit light in the silicon rich film, the luminescence observed in Fig. 5.17 is not necessarily due to the cerium ions, but possibly due to radiative defects produced after the 1200°C anneal. The reason for the lack of luminescence from these films is possibly the same reason given for the SRSN films; the emission from cerium ions also depends on oxygen.

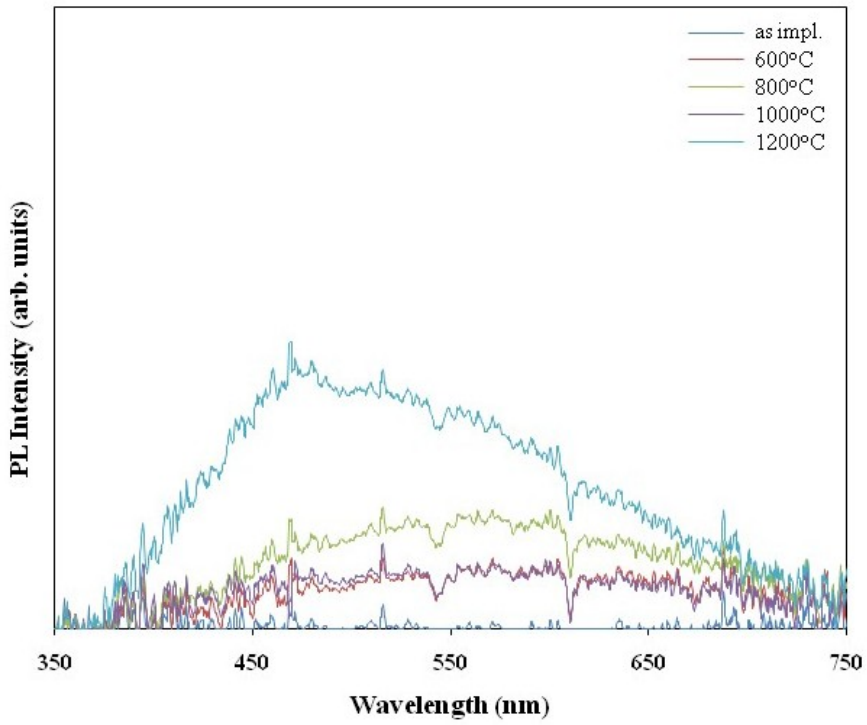

Figure 5.17: PL spectra of Ce-doped stoichiometric LPCVD film

5.2.2 XAS Results

The ICP-CVD grown Ce-doped films were analyzed with XAS at the Si *L* edge (2p excitation). Given that this was a silicon absorption edge, the information obtained pertains only to silicon bonded species in the film; information about the coordination and bonding environment of the cerium atoms was not accessible. The spectra from the two sets of samples are shown in Figs. 5.18 & 5.19.

One obvious feature that is present in both sets of samples is the double peak at ~106 eV. These are due to Si-O bonding [81] and are most likely from the surface where an oxide layer could have grown as they are also seen in the TEY signal (not shown). A couple of peaks which occur at ~109 eV and ~116 eV are also most likely due to Si-O bonding, but they will not be discussed any further. The shoulder at ~104 eV is due to Si-N bonding, while the peak at ~100 eV is due to Si-Si bonding [82].

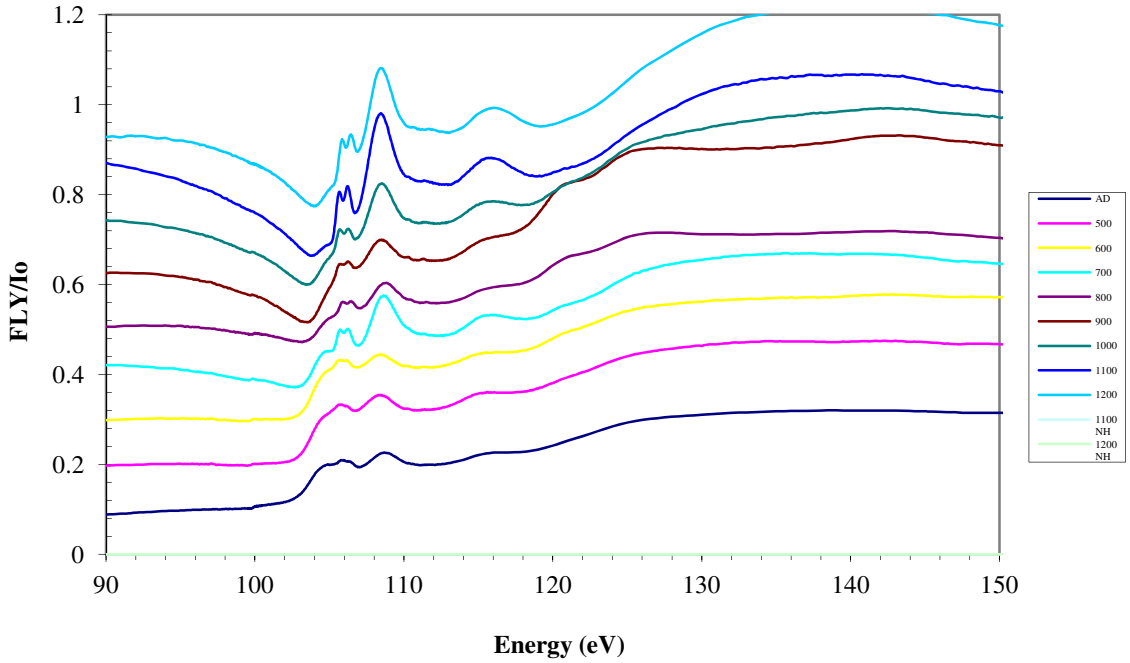

Figure 5.18: XAS spectra of Ce-doped stoichiometric silicon nitride samples

There is normally a shift in the Si-N peak to lower energies when there is a decrease in the amount of Si-N bonding to form Si-Si bonds. However, the shift is not seen in this data, which could mean that the silicon atoms are already clustered together post implantation and the creation of the silicon nanoclusters does not require breaking a significant number of Si-N bonds. In addition, the Si-N peak is not visible with annealing past ~800^{o}C as there is a dip in the spectrum that goes lower than the pre-edge. Though not conclusive, this dip has been attributed to x-ray scattering from voids [78], which provides further evidence to the TEM images in section 5.1.3 that there is void formation in the films. The voids could have been formed through implantation and grown with annealing, rather than been repaired by annealing as originally thought. If true, it is only after the voids reach a certain threshold size that the scattering effects begin to affect the XANES spectra with a dip.

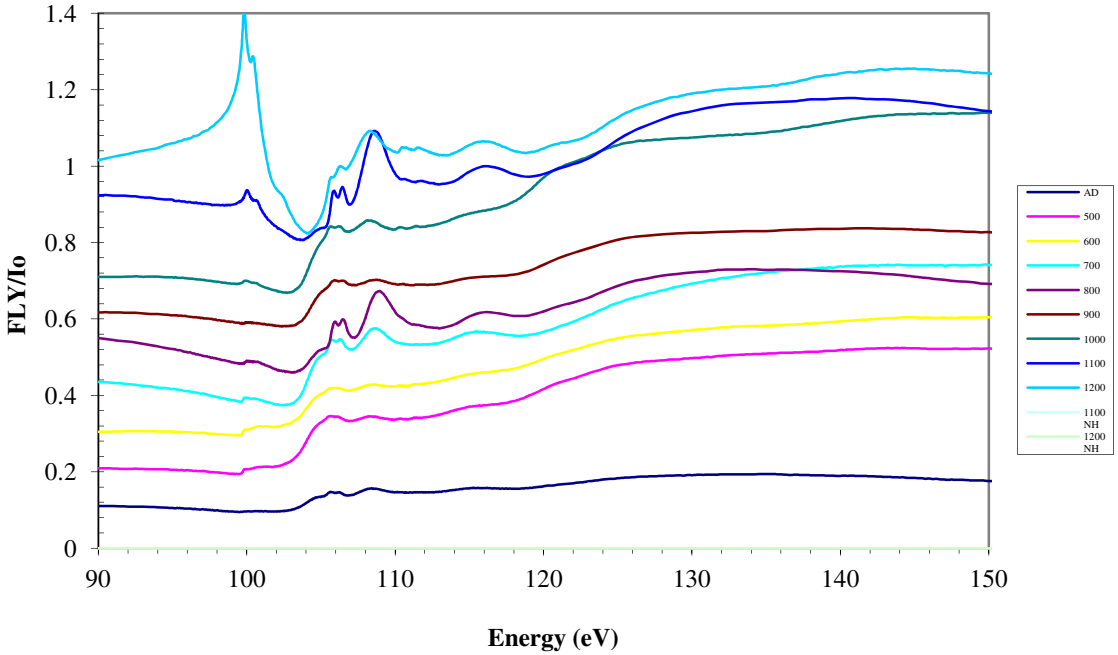

Figure 5.19: XAS of Ce-doped SRSN samples

The 100 eV Si-Si bond peak is only present in the spectra from the silicon rich films (Fig. 5.19). This makes sense as silicon nanoclusters were expected to be formed in only the silicon rich films. The peak is not present in the as-implanted film but appears after annealing and increases with higher anneal temperatures. This leads me to believe that though the silicon atoms may be clustered together in a Gaussian profile after implantation, they are not properly bonded together. Instead, they are most likely in interstitial sites. It is only after annealing that the nanoclusters form and the silicon atoms within them bond together; hence the appearance and increase of the Si-Si bonding peak. The large distorted peak seen after a 1200^{o}C anneal is most likely due to self absorption effects. This suggests that the nanoclusters are amorphous as this phenomenon is not evident in crystalline silicon. Additionally, this provides further evidence that though no nanoclusters were visible in any of the TEM images, this may have only been because they were amorphous and not because there were none present.

Chapter 6: Conclusions and Future Work

Using PL it was found that the SRSN films showed relatively bright luminescence attributed to silicon nanoclusters. The spectra of the dispersion ring and plasma samples were centred at about 750 nm and 650 nm, with the peak luminescence occurring after anneals of 600^{o}C and 800^{o}C respectively. Both spectra were redshifted at higher annealing temperatures. When the nitrogen was incorporated through the plasma the nitrogen was more easily incorporated into the film resulting in a higher nitrogen concentration, or in other words, the dispersion ring samples were more silicon rich than the plasma samples. The reason why the dispersion ring samples had lower energy emission was that the larger amount of excess silicon formed larger silicon nanoclusters in these films. Though the PL showed strong evidence of nanocluster formation, there was no conclusive evidence of their presence through TEM imaging.

A possible continuation of this project could concentrate on the electrical characterization of these films. If there is sufficient electroluminescence from the films, an LED structure could be made with a PIN junction and appropriate contacts.

The Ce-doped films exhibited even brighter luminescence than the SRSN films. Though the emission was for the most part from the Ce^{3+} ions, silicon nanoclusters were formed in the silicon rich which also contributed to the emission.

In the future, one could also investigate the electrical properties of these Ce-doped films. As well, it would be useful to perform XAS at a cerium absorption edge to obtain information about the bonding environment and coordination of the cerium ions.

References

[1] J.D. Plummer, M.D. Deal, and P.B. Griffin, *Silicon VLSI Technology: Fundamentals, Practice and Modeling*. Upper Saddle River, NJ: Prentice Hall, 2000.

[2] L. Pavesi and D.J. Lockwood, *Silicon Photonics*. New York: Springer, 2004.

[3] B. Jalali and S. Fathpour, "Silicon Photonics," *Lightwave Technology, Journal of*, vol. 24, no. 12, pp. 4600-4615, 2006.

[4] Z.T. Kang et al., "Synthesis of silicon quantum dot buried SiO_x films with controlled luminescent properties for solid-state lighting," *Nanotechnology*, vol. 17, no. 17, p. 4477, 2006.

[5] Intel, Silicon Photonics, http://techresearch.intel.com/articles/Tera-Scale/1419.htm, 2008.

[6] G.E. Moore, "Cramming More Components onto Integrated Circuits," *Electronics*, vol. 38, no. 8, pp. 114-117, 1965.

[7] L. Pavesi, "Will silicon be the photonic material of the third millenium?," *Journal of Physics: Condensed Matter*, vol. 15, no. 26, p. R1169, 2003.

[8] Transistor Count and Moore's Law – 2008, http://commons.wikimedia.org/wiki/File:Transistor_Count_and_Moore's_Law_-_2008_1024.png, 2008.

[9] "Interconnects," *International Technology Roadmap for Semiconductors*, 2003.

[10] A.G. Rickman, G.T. Reed, and F. Namavar, "Silicon-on-insulator optical rib waveguide loss and mode characteristics," *Lightwave Technology, Journal of*, vol. 12, no. 10, pp. 1771-1776, 1994.

[11] A. Liu et al., "A high-speed silicon optical modulator based on a metal-oxide-semiconductor capacitor," *Nature*, vol. 427, pp. 615-618, 2004.

[12] S.M. Csutak et al., "High-speed monolithically integrated silicon photoreceivers fabricated in 130-nm CMOS technology," *Lightwave Technology, Journal of*, vol. 20, no. 9, pp. 1724-1729, 2002.

[13] L.T. Canham, "Silicon quantum wire array fabrication by electrochemical and chemical dissolution of wafers," *Applied Physics Letters*, vol. 57, no. 10, pp. 1046-1048, 1990.

[14] T. Shimizu-Iwayama et al., "Visible photoluminescence related to Si precipitates in Si^+-implanted SiO_2," *Journal of Physics: Condensed Matter*, vol. 5, no. 31, p. L375, 1993.

[15] L. Pavesi et al., "Optical gain in silicon nanocrystals," *NATURE*, vol. 408, no.

[16] N.-M. Park et al., "Quantum Confinement in Amorphous Silicon Quantum Dots Embedded in Silicon Nitride," *Phys. Rev. Lett.*, vol. 86, no. 7, pp. 1355-1357, 2001.

[17] L.-Y. Chen, W.-H. Chen, and F.C.-N. Hong, "Visible electroluminescence from silicon nanocrystals embedded in amorphous silicon nitride matrix," *Applied Physics Letters*, vol. 86, no. 19, p. 193506, 2005.

[18] A.J. Kenyon, "Recent developments in rare-earth doped materials for optoelectronics," *Progress in Quantum Electronics*, vol. 26, no. 4-5, pp. 225-284, 2002.

[19] N.W. Ashcroft and N.D. Mermin, *Solid State Physics*. Belmont, CA: Brooks/Cole, 1976.

[20] J.R. Chelikowsky and M.L. Cohen, "Nonlocal pseudopotential calculations for the electronic structure of eleven diamond and zinc-blende semiconductors," *Phys. Rev. B*, vol. 14, no. 2, pp. 556-582, 1976.

[21] B.E.A. Saleh and M.C. Teich, *Fundamentals of Photonics*. Hoboken, NJ: John Wiley & Sons, Inc., 1991.

[22] P.Y. Yu and M. Cardona, *Fundamentals of Semiconductors: Physics and Materials Properties*, 4th ed. Berlin: Springer-Verlag, 2010.

[23] C. Kittel, *Introduction to Solid State Physics*, 7th ed. Hoboken, NJ: John Wiley & Sons, Inc., 1996.

[24] D. Kovalev et al., "Breakdown of the k-Conservation Rule in Si Nanocrystals," *Phys. Rev. Lett.*, vol. 81, no. 13, pp. 2803-2806, 1998.

[25] L. Brus, "Electronic wave functions in semiconductor clusters: experiment and theory," *The Journal of Physical Chemistry*, vol. 90, no. 12, pp. 2555-2560, 1986.

[26] L. Brus, "Zero-dimensional "excitons" in semiconductor clusters," *Quantum Electronics, IEEE Journal of*, vol. 22, no. 9, pp. 1909-1914, 1986.

[27] J.P. Proot, C. Delerue, and G. Allan, "Electronic structure and optical properties of silicon crystallites: Application to porous silicon," *Applied Physics Letters*, vol. 61, no. 16, pp. 1948-1950, 1992.

[28] M.V. Wolkin et al., "Electronic States and Luminescence in Porous Silicon Quantum Dots: The Role of Oxygen," *Phys. Rev. Lett.*, vol. 82, no. 1, pp. 197-200, 1999.

[29] A.D. Yoffe, "Semiconductor quantum dots and related systems: Electronic, optical, luminescence and related properties of low dimensional systems," *Advances in Physics*, vol. 50, no. 1, p. 208, 2001.

[30] N. Daldosso et al., "Silicon nanocrystal formation in annealed silicon-rich silicon oxide films prepared by plasma enhanced chemical vapor deposition," *Journal of Applied Physics*, vol. 101, no. 11, p. 113510, 2007.

[31] T. Komoda et al., "Visible photoluminescence at room temperature from microcrystalline silicon precipitates in SiO_2 formed by ion implantation," *Nuclear Instruments and Methods in Physics Research Section B: Beam Interactions with Materials and Atoms*, vol. 96, no. 1-2, pp. 387-391, 1995.

[32] P. Mutti et al., "Room-temperature visible luminescence from silicon nanocrystals in silicon implanted SiO_2 layers," *Applied Physics Letters*, vol. 66, no. 7, pp. 851-853, 1995.

[33] L.-S. Liao et al., "Blue luminescence from Si^+-implanted SiO_2 films thermally grown on crystalline silicon," *Applied Physics Letters*, vol. 68, no. 6, pp. 850-852, 1996.

[34] X. Wen, L.V. Dao, and P. Hannaford, "Temperature dependence of photoluminescence in silicon quantum dots," *Journal of Physics D: Applied Physics*, vol. 40, no. 12, p. 3573, 2007.

[35] H.Z. Song and X.M. Bao, "Visible photoluminescence from silicon-ion-implanted SiO_2 film and its multiple mechanisms ," *Phys. Rev. B*, vol. 55, no. 11, pp. 6988-6993, 1997.

[36] H. Nishikawa et al., "Photoluminescence study of defects in ion-implanted thermal SiO_2 films," *Journal of Applied Physics*, vol. 78, no. 2, pp. 842-846, 1995.

[37] F. Iacona et al., "Formation and evolution of luminescent Si nanoclusters produced by thermal annealing of SiO_x films," *Journal of Applied Physics*, vol. 95, no. 7, pp. 3723-3732, 2004.

[38] S.V. Deshpande et al., "Optical properties of silicon nitride films deposited by hot filament chemical vapor deposition," *Journal of Applied Physics*, vol. 77, no. 12, pp. 6534-6541, 1995.

[39] M. Zacharias et al., "Size-controlled highly luminescent silicon nanocrystals: A SiO/SiO_2 superlattice approach," *Applied Physics Letters*, vol. 80, no. 4, pp. 661-663, 2002.

[40] S. Im et al., "Enhancing defect-related photoluminescence by hot implantation into SiO_2 layers," *Applied Physics Letters*, vol. 74, no. 7, pp. 961-963, 1999.

[41] M.-S. Yang et al., "Effect of nitride passivation on the visible photoluminescence from Si-nanocrystals," *Applied Physics Letters*, vol. 85, no. 16, pp. 3408-3410, 2004.

[42] T.-Y. Kim et al., "Quantum confinement effect of silicon nanocrystals in situ grown in silicon nitride films," *Applied Physics Letters*, vol. 85, no. 22, pp. 5355-5357, 2004.

[43] L. Dal Negro et al., "Light emission efficiency and dynamics in silicon-rich silicon nitride films," *Applied Physics Letters*, vol. 88, no. 23, p. 233109, 2006.

[44] F.L. Bregolin et al., "Photoluminescence induced by Si implantation into Si_3N_4 matrix," *Nuclear Instruments and Methods in Physics Research Section B: Beam Interactions with Materials and Atoms*, vol. 267, no. 8-9, pp. 1314-1316, 2009.

[45] M.L. Brongersma et al., "Size-dependent electron-hole exchange interaction in Si nanocrystals," *Applied Physics Letters*, vol. 76, no. 3, pp. 351-353, 2000.

[46] M. Wang et al., "Photoluminescence of Si-rich silicon nitride: Defect-related states and silicon nanoclusters," *Applied Physics Letters*, vol. 90, no. 13, p. 131903, 2007.

[47] B.-H. Kim et al., "Photoluminescence of silicon quantum dots in silicon nitride grown by NH_3 and SiH_4," *Applied Physics Letters*, vol. 86, no. 9, p. 091908, 2005.

[48] C.-H. Cho et al., "Effect of hydrogen passivation on charge storage in silicon quantum dots embedded in silicon nitride film," *Applied Physics Letters*, vol. 86, no. 14, p. 143107, 2005.

[49] A. Irrera et al., "Electroluminescence properties of light emitting devices based on silicon nanocrystals," *Physica E: Low-dimensional Systems and Nanostructures*, vol. 16, no. 3-4, pp. 395-399, 2003.

[50] S. Prezioso et al., "Electrical conduction and electroluminescence in nanocrystalline silicon-based light emitting devices," *Journal of Applied Physics*, vol. 104, no. 6, p. 063103, 2008.

[51] G. Franzò, V. Vinciguerra, and F. Priolo, "The excitation mechanism of rare-earth ions in silicon nanocrystals," *Applied Physics A: Materials Science & Processing*, vol. 69, pp. 3-12, 1999.

[52] A.J. Kenyon et al., "Luminescence from erbium-doped silicon nanocrystals in silica: Excitation mechanisms," *Journal of Applied Physics*, vol. 91, no. 1, pp. 367-374, 2002.

[53] P.G. Kik and A. Polman, "Exciton--erbium interactions in Si nanocrystal-doped SiO_2," *Journal of Applied Physics*, vol. 88, no. 4, pp. 1992-1998, 2000.

[54] C.E. Chryssou et al., "Evidence of energy coupling between Si nanocrystals and Er^{3+} in ion-implanted silica thin films," *Applied Physics Letters*, vol. 75, no. 14, pp. 2011-2013, 1999.

[55] J. Li et al., "The formation of light emitting cerium silicates in cerium-doped silicon oxides," *Applied Physics Letters*, vol. 94, no. 1, p. 011112, 2009.

[56] L. Guerbous and O. Krachni, "The 4f-5d luminescence transitions in cerium-doped LuF_3," *Journal of Modern Optics*, vol. 53, no. 14, pp. 2043-2053, 2006.

[57] T. Roschuk et al., "Optical and compositional characterization of SiO_xN_y and SiO_x thin films deposited by electron cyclotron resonance plasma enhanced chemical vapor deposition," *Journal of Vacuum Science & Technology A: Vacuum, Surfaces, and Films*, vol. 22, no. 3, pp. 883-886, 2004.

[58] X.D. Pi et al., "Light emission from Si nanoclusters formed at low temperatures," *Applied Physics Letters*, vol. 88, no. 10, p. 103111, 2006.

[59] T. Shimizu-Iwayama et al., "Visible photoluminescence in Si^+-implanted silica glass," *Journal of Applied Physics*, vol. 75, no. 12, pp. 7779-7783, 1994.

[60] N. Lalic and J. Linnros, "Light emitting diode structure based on Si nanocrystals formed by implantation into thermal oxide," *Journal of Luminescence*, vol. 80, no. 1-4, pp. 263-267, 1998.

[61] G.-R. Lin et al., "Oxygen defect and Si nanocrystal dependent white-light and near-infrared electroluminescence of Si-implanted and plasma-enhanced chemical-vapor deposition-grown Si-rich SiO_2," *Journal of Applied Physics*, vol. 97, no. 9, p. 094306, 2005.

[62] G. Dearnaley, *Ion Implantation*.: American Elsevier Publishing Company, Inc., 1973.

[63] A. Fiory, "Recent developments in rapid thermal processing," *Journal of Electronic Materials*, vol. 31, pp. 981-987, 2002.

[64] M. Ohring, *Materials Science of Thin Films*, 2nd ed. Hoboken, NJ: Academic Press, 2002.

[65] L. da Silva, R.D. Mansano, and R. Furlan, "Silicon nitride deposited by inductively coupled plasma using silane and nitrogen," *Vacuum*, vol. 65, no. 2, pp. 213-220, 2002.

[66] G.S. Anderson, W.N. Mayer, and G.K. Wehner, "Sputtering of Dielectrics by High-Frequency Fields," *Journal of Applied Physics*, vol. 33, no. 10, pp. 2991-2992, 1962.

[67] J. Hopwood, "Review of inductively coupled plasmas for plasma processing," *Plasma Sources Science and Technology*, vol. 1, no. 2, p. 109, 1992.

[68] H. Zhang, "Study of the optimal deposition conditions for an inductively coupled plasma chemical vapour deposition (ICP-CVD) system," McMaster University, 2005.

[69] D.G. Ashworth, R. Oven, and B. Mundin, "Representation of ion implantation profiles by Pearson frequency distribution curves," *Journal of Physics D: Applied Physics*, vol. 23, no. 7, p. 870, 1990.

[70] T.S. Iwayama et al., "Control of embedded Si nanocrystals in SiO_2 by rapid thermal annealing and enhanced photoluminescence characterization," *Surface and Coatings Technology*, vol. 201, no. 19-20, pp. 8490-8494, 2007.

[71] University of Western, Tandetron Accelerator Laboratory, http://www.uwo.ca/isw/facilities/Tandetron/index.htm.

[72] B.G. Streetman and S.K. Banerjee, *Solid State Electronic Devices*, 6th ed. Upper Saddle River, NJ: Pearson Prentice Hall, 2006.

[73] O.H.Y. Zalloum et al., "Laser photoluminescence spectrometer based on charge-coupled device detection for silicon-based photonics," *Review of Scientific Instruments*, vol. 77, no. 2, p. 023907, 2006.

[74] D.B. Williams and C.B. Carter, *Transmission Electron Microscopy: A Textbook for Materials Science*. New York: Springer, 2009.

[75] H. Foll, Transmission Electron Microscopy, http://www.tf.uni-kiel.de/matwis/amat/def_en/kap_6/backbone/r6_3_1.html.

[76] B.K. Agarwal, *X-Ray Spectroscopy An Introduction*, 2nd ed. New York: Springer-Verlag, 1991.

[77] Canadian Light Source, VLS-PGM Beamline, http://exshare.lightsource.ca/vlspgm/Pages/default.aspx.

[78] P. Wilson et al., "Effect of thermal treatment on the growth, structure and luminescence of nitride-passivated silicon nanoclusters," *Nanoscale Research Letters*, vol. 6, pp. 1-12, 2011.

[79] B.-H. Kim, R.F. Davis, and S.-J. Park, "Optical property of silicon quantum dots embedded in silicon nitride by thermal annealing," *Thin Solid Films*, vol. 518, no. 6, pp. 1744-1746, 2010.

[80] S. Cheylan and R.G. Elliman, "Effect of hydrogen on the photoluminescence of Si nanocrystals embedded in a SiO_2 matrix," *Applied Physics Letters*, vol. 78, no. 9, pp. 1225-1227, 2001.

[81] M. Kasrai et al., "Sampling depth of total electron and fluorescence measurements in Si L- and K-edge absorption spectroscopy," *Applied Surface Science*, vol. 99, no. 4, pp. 303-312, 1996.

[82] Y. Baba, H. Yamamoto, and T.A. Sasaki, "Surface x-ray-absorption fine structures of SiO_x ($0<x<2$) and SiN_x ($0<x<4/3$) produced by low-energy ion implantation in Si(100)," *Phys. Rev. B*, vol. 48, no. 15, pp. 10972-10977, 1993.